chemosensors

Article

Pulse Sensors Based on Laser-Induced Graphene Transferred to Biocompatible Polyurethane Networks: Fabrication, Transfer Methods, Characterization, and Application

Vanja Vojnović *, Marko Spasenović, Ivan Pešić, Teodora Vićentić, Milena Rašljić Rafajilović, Stefan D. Ilić and Marija V. Pergal *

Center for Microelectronic Technologies, Institute of Chemistry, Technology and Metallurgy—National Institute of the Republic of Serbia, Njegoševa 12, 11000 Belgrade, Serbia; marko.spasenovic@ihtm.bg.ac.rs (M.S.); ivan.pesic@ihtm.bg.ac.rs (I.P.); teodora.vicentic@ihtm.bg.ac.rs (T.V.); milena.rasljic@ihtm.bg.ac.rs (M.R.R.); stefan.ilic@ihtm.bg.ac.rs (S.D.I.)

* Correspondence: marija.pergal@ihtm.bg.ac.rs (M.V.P.); vanja.vojnovic@ihtm.bg.ac.rs (V.V.)

Abstract: Flexible, wearable biomedical sensors based on laser-induced graphene (LIG) have garnered significant attention due to a straightforward fabrication process and exceptional electrical and mechanical properties. However, most relevant studies rely on commercial polyimide precursors, which suffer from inadequate biocompatibility and weak adhesion between the precursor material and the LIG layer. To address these challenges, we synthesized cross-linked polyurethanes (PUs) with good biocompatibility and used them as substrates for LIG-based wearable pulse sensors. During fabrication, we employed two methods of LIG transfer to achieve optimal transfer yield. We adjusted the thickness of PU films and tailored their mechanical and physicochemical properties by varying the soft segment content to achieve optimal sensor performance. Our findings demonstrate that the success of LIG transfer is strongly influenced by the structure and composition of the polymeric substrate. Tensile testing revealed that increasing the soft segment content in PU films significantly improved their tensile strength, elongation at break, and flexibility, with PU based on 50 wt.% soft segment content (PU-50) showing the best mechanical properties. LIG exhibited minimal sensitivity to humidity, while PU films maintained high transparency (>80% at 500 nm), and PU-50 was non-toxic, with less than 5% lactate dehydrogenase (LDH) release in endothelial cell cultures, confirming its biocompatibility. Adhesion tests demonstrated that LIG transferred onto PU-50 exhibited significantly stronger adhesion compared to other tested substrates, with only a 30% increase in electrical resistance after the Scotch tape test, ensuring stability for wearable sensors. The optimal substrate, a semicrystalline PU-50, yielded superior transfer efficiency. Among all tested sensors, the LIG/PU-50, featuring a 77 μm thick substrate with good mechanical properties and improved adhesion, exhibited the highest signal-to-noise ratio (SNR). This study showcases a skin-safe LIG/PU-based pulse sensor that has significant potential for applications as a wearable patch in medical and sports monitoring.

Keywords: flexible wearable sensor; pulse sensor; laser-induced graphene; biocompatible polyurethane; structure–property relationship

check for updates

Received: 26 December 2024
Revised: 20 March 2025
Accepted: 26 March 2025
Published: 2 April 2025

Citation: Vojnović, V.; Spasenović, M.; Pešić, I.; Vićentić, T.; Rašljić Rafajilović, M.; Ilić, S.D.; Pergal, M.V. Pulse Sensors Based on Laser-Induced Graphene Transferred to Biocompatible Polyurethane Networks: Fabrication, Transfer Methods, Characterization, and Application. *Chemosensors* **2025**, *13*, 122. https://doi.org/10.3390/chemosensors13040122

Copyright: © 2025 by the authors. Licensee MDPI, Basel, Switzerland. This article is an open access article distributed under the terms and conditions of the Creative Commons Attribution (CC BY) license (https://creativecommons.org/licenses/by/4.0/).

1. Introduction

Health monitoring devices, such as heartbeat sensors, have become integral to everyday life. There is a growing emphasis on developing flexible, reliable, and cost-effective

wearable devices for real-time tracking of human physiological parameters [1–4]. Heart rate is one of the most essential physiological parameters, as it provides critical insights into cardiovascular health and overall well-being. Due to the significance of heart rate, many scientific studies are aimed at developing novel, cost-effective, biocompatible, and reliable heart rate sensors for continuous health monitoring [5–7]. A critical aspect of these devices is the ability to tune the properties of both the sensing material and the supporting substrates. Laser-induced graphene (LIG) is emerging as an interesting material because it is flexible, tunable, and can be made on a variety of substrates [8–11]. LIG has gained attention as an active material for biomedical applications, including piezoresistive strain sensors for heartbeat monitoring [5,12–17] and chemical biosensing [18–20].

LIG can be successfully fabricated on many types of natural [9,11,21,22] and synthetic [8,10,14,23,24] materials with sufficient carbon content. The underlying mechanism mainly involves carbonization and graphenization of the substrate surface, with the resulting porous structure of LIG attributed to the rapid release of gasses, such as CO, NO, H_2, and water vapor [8,25,26]. A key advantage of this method is the direct conversion of carbon-containing materials into LIG in the air. This direct scribing approach enables fast, one-step production of graphene or graphene-like material with customizable shapes and dimensions on various synthetic polymers structurally similar to commercially available polyimide (PI) [10,23,24], as well as naturally occurring polymers like cellulose or lignin [21,22]. Additionally, composites such as poly(dimethylsiloxane) (PDMS) with PI particles [27,28], tetraethylene glycol (TEG) [29], poly(ether ether ketone) (PEEK) [30], and Triton X-100 [31] have also been found suitable for LIG production. For some carbon-rich materials like activated carbon, cork, coconut shells, or potato skins, multiple lasing or time-saving lasing with a defocus method are often required to generate LIG [9]. Researchers have developed strategies, such as heteroatom and nanoparticle doping of LIG [32,33], to enhance material properties for specific applications.

Different mechanisms for LIG formation, including photothermal, photochemical, or hybrid, processes have been proposed [34,35]. Comprehensive molecular dynamics simulations using ReaxFF have provided valuable insights into the LIG formation on diverse precursors under UV or IR laser irradiation [25,26,36,37]. The physical properties and morphology of LIG can be fine-tuned by altering laser parameters [38,39], while the wettability of the LIG surface can be changed by laser induction under different atmospheric conditions [40].

Polyurethanes (PUs) have emerged as promising candidates for wearable sensor substrates due to their unique combination of properties, including chemical corrosion resistance [41], durability, strong adhesion, good thermal and oxidative stability [42], simple production process, good mechanical flexibility, good biocompatibility and non-toxicity [43], long-term and conformal attachment to the skin (>72 h) [44]. These attributes have led to the widespread use of PUs in clothing fabrics, aerospace, medical devices and implants, biomedical tissue engineering, and wound healthcare applications [44,45]. Cross-linked PUs are typically synthesized via polyaddition reactions involving macrodiols, diisocyanates, and crosslinking agents [46]. By varying the soft segment (SS) and hard segment (HS) content, as well as the choice of starting reactants, the mechanical and physicochemical properties of PUs can be tailored for specific applications [47]. Incorporating poly(dimethylsiloxane) (PDMS) macrodiol as the soft segment into PU networks imparts beneficial properties, such as non-toxicity, hydrophobicity, and elasticity [41].

Commercial PI film is the most common substrate for the formation of high-quality LIG [8,14,38,48], ascribing to its thermal and mechanical stability and high carbon content. Nonetheless, suboptimal biocompatibility and stretchability of PI necessitate transferring LIG from PI onto alternative substrates to meet the demands of wearable electronics.

LIG was successfully transferred onto PDMS to create biocompatible, flexible devices for direct skin application in heartbeat monitoring [14,17]. Despite many research studies on LIG-based sensors, usually on PI, the biocompatibility of the substrates used in these systems remains underexplored. Our study addresses this gap by focusing on synthesizing biocompatible polymer substrates with good mechanical properties [43] for our LIG-based pulse wearable sensors. These PDMS-based PUs are biocompatible [43], skin-safe, and can be used in moisture conditions [41], making them suitable for direct skin contact in humid environments. Additionally, synthetic polymers offer the potential for customizing the thickness of supporting materials, a crucial factor for strain sensors designed to detect deformations induced by low forces [12], such as heartbeat.

For wearable device applications, strong adhesion [49] between the supporting substrate and LIG is essential to ensure material durability in working conditions. However, LIG fabricated directly on precursor materials often fails to meet basic Scotch tape test standards [8]. To address this limitation, the transfer of LIG to other substrates has been widely explored, enabling the integration of LIG onto various substrates, including PDMS [14,49,50]. The transfer method is particularly advantageous when the target substrate lacks aromatic structures or carbon sources, rendering it unsuitable for direct LIG generation, as is the case with materials like PUs, Teflon, or Nylon 6,6 [9]. Researchers have investigated diverse strategies for transferring LIG produced on an original precursor to various elastomers and thermoplastic polymers, both with [51–53] or without adhesive layers [54,55]. This capability facilitates the development of LIG-based flexible and transparent electronic devices. Typically, the transfer process involves pouring liquid, uncured polymer onto the LIG/PI. The polymer infiltrates the LIG structure through gravity, vacuum assistance, applied pressure [49,54], hot compression [16,56], or lamination for commercial thermoplastic polymers [55]. Once the polymer solidifies, LIG becomes bonded to the new substrate and can be peeled off from the parent substrate.

The transfer approach is primarily applied to commercial polymeric tapes [51,53], PDMS elastomers [14,50,57,58], silicone rubber [59], poly(methyl 2-methyl propanoate) (PMMA) [54], poly(ethylene terephthalate) (PET) [52], biodegradable waterborne PU [60], polystyrene-*block*-poly (ethylene butylene)-*block*-polystyrene (SEBS) [16], and poly(lactic acid) (PLA) [56] using various physical and chemical methods. An innovative method involves the cryogenic transfer of LIG to hydrogel films [61]. Li et al. [55] reported that the efficiency of LIG transfer depends on the polymer type. For instance, some polymers selectively transfer the LIG carpet morphology, producing fibrous surface microstructures, like the LIG/low-density polyethylene composites, while others, like the LIG/polypropylene composites, transfer the basal LIG foam layer, resulting in porous foam-like surface structures.

Despite the promising features of LIG, integrating it into biocompatible substrates for wearable applications remains a considerable challenge. Dallinger et al. [53] successfully transferred LIG from PI onto a medical-grade polyurethane (MPU) patch using an adhesive layer and applied pressure, achieving outstanding stretchability (>100%) and long-term stability in electromechanical tensile tests. Ultimately, transferring LIG from a PI substrate to a stretchable elastomer offers a promising approach for the development of soft, skin-compatible electronics. To address skin irritation issues, we propose the use of a novel, synthesized biocompatible substrate for LIG-based sensors, optimized for stability in humid conditions [41].

In this study, our innovative approach involves developing pulse sensors based on LIG on the surface of novel biocompatible polyurethane (PU) networks. A series of PUs with varying soft segment content (30, 40, and 50 wt.%) were synthesized using α,ω-dihydroxyethoxy-poly(dimethylsiloxane) as the soft segment, 4,4′-methylenediphenyl diisocyanate, and hydroxy-functional hyperbranched polyester (HBP) as the hard segment. Namely,

we explored LIG production on a commercially available polyimide (PI) film, commonly used for LIG production, followed by the transfer of LIG onto PU films. The soft segment content and thickness of the PU films were adjusted to achieve optimal sensor performance. Two different transfer methods were applied: spin coating and stamping. Thin films of LIG and PUs were characterized by UV-VIS spectroscopy, Fourier-transform infrared (FTIR) spectroscopy, scanning electron microscopy (SEM) with an energy-dispersive X-ray spectrometer (EDX), transmission electron microscopy (TEM), Raman spectroscopy, X-ray diffraction (XRD), nanoindentation, tensile testing, adhesion tape test, cytotoxicity test, humidity interference, and electrical measurements. LIG devices on PU substrates were connected to a pulse simulator and a Keithley 2450 Source Measure Unit for electrical measurements in order to examine pulse sensing with these novel LIG-based materials.

2. Materials and Methods

2.1. Materials

Two types of commercial polyimide (PI) Kapton® HN tapes (sheet and adhesive tape) were obtained from DuPont (Wilmington, DE, USA), each with a thickness of 76 μm.

For the synthesis of the cross-linked polyurethanes in the present work, the following reactants and reagents were used: 4,4′-methylene diphenyl diisocyanate (MDI, >98% purity) and Boltorn® (Perstorp, Sweden) aliphatic hyperbranched polyester of the second pseudo-generation with hydroxyl end groups (HBPs), both as the hard segment component; α,ω-dihydroxy-(ethylene oxide-poly(dimethylsiloxane)-ethylene oxide) (EO-PDMS; M_n = 1000 g/mol, Gelest, Frankfurt, Germany) as the soft segment; *N*-methyl-2-pyrrolidone (NMP, 99% purity) and tetrahydrofuran (THF, 98% purity) were used as solvents; and stannous-octoate ($Sn(Oct)_2$, 98% purity) was used as the catalyst.

MDI, purchased from Sigma Aldrich (St. Louis, MI, USA) with an isocyanate content of 33.6 wt.% (determined by the standard dibutylamine back-titration method [62]), was stored in a refrigerator and used as received. HBP (M_n = 1749 g/mol and 16 hydroxyl end groups) was procured from Perstorp Speciality Chemicals AB (Perstorp, Sweden) and dried under vacuum for 5 h at 50 °C prior to use.

The solvents, NMP (Thermo Scientific Chemical, Waltham, MA, USA) and THF (Fisher Chemical, Pittsburgh, PA, USA), were purified via distillation over calcium hydride (Sigma Aldrich, St. Louis, MI, USA) and lithium aluminum hydride (Sigma Aldrich, St. Louis, MI, USA), respectively. The anhydrous, distilled solvents were subsequently stored over molecular sieves (0.4 nm) in dark glass bottles and used for each synthesis. After purification, both anhydrous and distilled solvents were stored over molecular sieves (0.4 nm) in dark glass bottles and used for each synthesis. $Sn(Oct)_2$, also sourced from Sigma Aldrich, was dissolved in a 1:1 (v/v) mixture of NMP and THF to prepare a catalyst solution for the reaction.

2.2. Laser-Induced Graphene Production

The precursor used for the direct production of LIG for transfer via spin coating was Kapton® adhesive tape, and the precursor used for transfer via stamping and for pulse sensing was a Kapton® sheet without an adhesive layer.

A commercial, low-cost, continuous CO_2 laser was employed to fabricate LIG under ambient conditions. Based on previous research [14], optimal lasing parameters were established to ensure high-quality LIG formation. The laser parameters used for LIG production on the polyimide film were a power setting of 20% (12 W), a scanning speed of 600 mm/s, and a resolution of 900 DPI. The PI precursor was fixed onto a silicon wafer, and rectangular LIG patterns (2 cm × 1 cm) were directly scribed onto the commercial polyimide films.

2.3. Synthesis of Polyurethanes

Cross-linked polyurethanes with varying soft segment content (PU-30, PU-40, and PU-50, where numbers represent the wt.% of SSC) were synthesized via a two-step polyaddition in solution under an inert atmosphere. The soft segment (SS) in polyurethanes refers to the flexible polymer chains, such as poly(dimethylsiloxane), that impart elasticity and hydrophobicity to the material. The "soft segment content" (SSC) is defined as the ratio of the mass of macrodiol chains without terminal hydroxyl groups to the total mass of the polymer, usually expressed as a percentage [63]. The molar ratio of −NCO (from MDI) to −OH (from EO-PDMS prepolymer and HBP) groups was maintained at 1.05, and the $Sn(Oct)_2$ concentration was set at 0.15 mol% per mole of EO-PDMS prepolymer. The synthesis procedure for PU-50 is exemplarily described here as a representative example, with the same protocol followed for PU-30 and PU-40. For the first phase of the reaction, the following reactants and solvents were added to a four-neck, round bottom flask equipped with a reflux condenser: 3.0000 g of EO-PDMS, 2 mL of THF and 16 mL of NMP, and 1.5750 g of MDI in order to prepare NCO-terminated prepolymer. The reaction mixture was stirred at room temperature using a mechanical stirrer, while a silicon oil bath with an immersed thermometer was used for temperature control. Once the temperature reached 50 °C, 10 µL of the freshly prepared $Sn(Oct)_2$ catalyst solution was added, marking the beginning of the first phase of the reaction. Meanwhile, solutions for the second phase of polyaddition were prepared: 1.0616 g of HBP was sonicated in 5 mL of NMP, and 0.4625 g of MDI was dissolved in 2 mL of NMP. After 30 min of stirring the reaction mixture at 50 °C, the prepared solutions of HBP and then MDI were slowly added dropwise to the NCO-terminated prepolymer, initiating the second reaction phase. During this phase, the temperature was increased to 60 °C, and the reaction mixture was stirred for approximately 20 min until the desired viscosity was achieved for the spin coating and stamping methods. The viscosity of the polyurethane (PU) reaction mixture plays a critical role in setting the final thickness of the coated layer. During synthesis, the viscosity of each sample was adjusted to achieve a honey-like consistency before film preparation via spin coating. The crosslinking rate was directly influenced by the PU composition (30, 40, and 50 wt.%), which, in turn, affected the viscosity of the reaction mixture and, consequently, the resulting film thickness. Specifically, PU-30 and PU-40 exhibited significantly faster crosslinking compared to PU-50, leading to higher viscosity in the reaction mixture and, consequently, thicker films. Figure 1 illustrates the simplified chemical structure of the synthesized PU network.

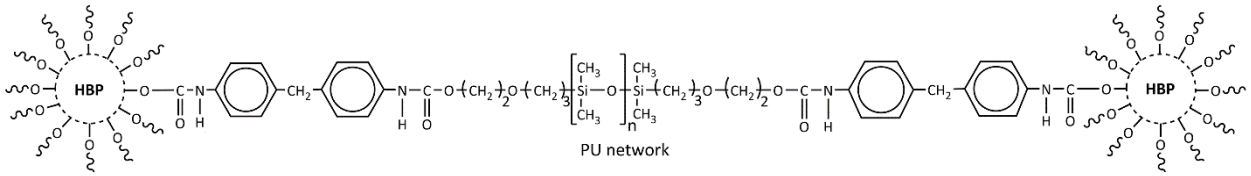

Figure 1. Simplified chemical structure of the synthesized biocompatible cross-linked PU.

2.3.1. LIG Transfer Via the Spin Coating Method

Polyurethane layers were deposited onto LIG/PI substrates, which were fixed to silicon wafers using the spin coating technique. This process enabled the transfer of LIG from PI to PUs with 30, 40, and 50 wt.% of SSC. The transfer was completely successful on the PU-50 substrate, partially successful on PU-40, and limited on PU-30.

Spin coating was performed at speeds ranging from 200 to 1000 rpm, during which ~2 mL of the reaction mixture was deposited for 30 s. The coated layer was then baked on a hot plate at 90 °C for 2 min. The described procedure was repeated for each layer, after which the PU film underwent a final curing process on a hot plate at 90 °C for 1 h.

Once curing was complete, the coated PU films were carefully peeled off, completing the LIG transfer. Figure 2 depicts photographs of the spin coating process, highlighting the successful LIG transfer onto the PU-50 substrate.

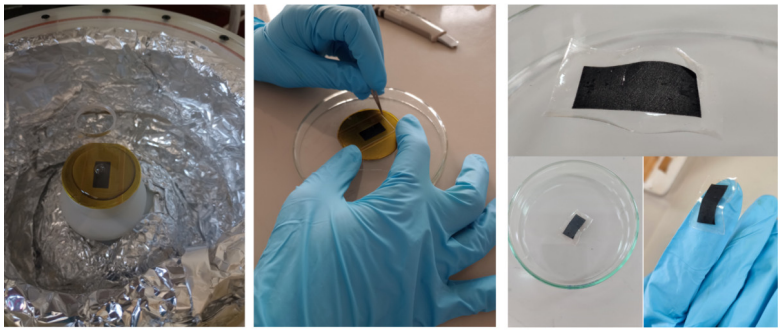

Figure 2. Photographs of (**a**) the transferring procedure using the spin coating method and (**b**) successfully transferred LIG on the PU-50 substrate.

The resulting LIG/PU materials obtained Via the spin coating were designated as follows:

- LIG/PU-50_{lo}: LIG transferred onto a 77 µm thick PU-50 substrate;
- LIG/PU-50_{hi}: LIG transferred onto an 88 µm thick PU-50 substrate;
- LIG/PU-40: LIG transferred onto a 100 µm thick PU-40 substrate;
- LIG/PU-30_{sc}: LIG transferred via spin coating onto a 100 µm thick PU-30 substrate.

2.3.2. LIG Transfer Via the Stamping Method

Another type of sample was prepared by transferring LIG onto PU with 30 wt.% SSC (PU-30) using the stamping method. In this approach, the reaction mixture was poured into a Teflon® (Termoplast, Belgrade, Serbia) mold, and the samples were cured in an air-circulating oven using a multi-step protocol: 2 h at 40 °C, 2 h at 60 °C, and 12 h at 80 °C. This curing procedure minimized solvent evaporation and prevented bubble formation in the PU sample. This procedure was used to obtain semi-cured and still sticky PU-30, which would facilitate LIG transfer from DuPont™ Kapton® sheet to PU-30. This method resulted in a uniform transfer of LIG on PU-30 as compared to the spin coating method, as illustrated in Figure 3. Material obtained via the stamping method was designated as LIG/PU-30st.

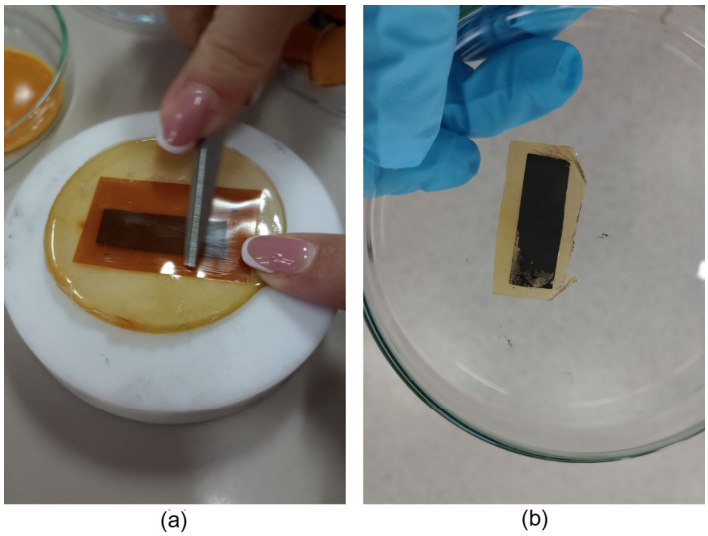

Figure 3. Photographs of the stamping procedure: (**a**) LIG transfer from commercial PI onto semi-cured PU-30 through manual pressure, and (**b**) successful LIG transfer on PU-30st.

Figure 4 illustrates the full fabrication process, including both spin coating and stamping methods.

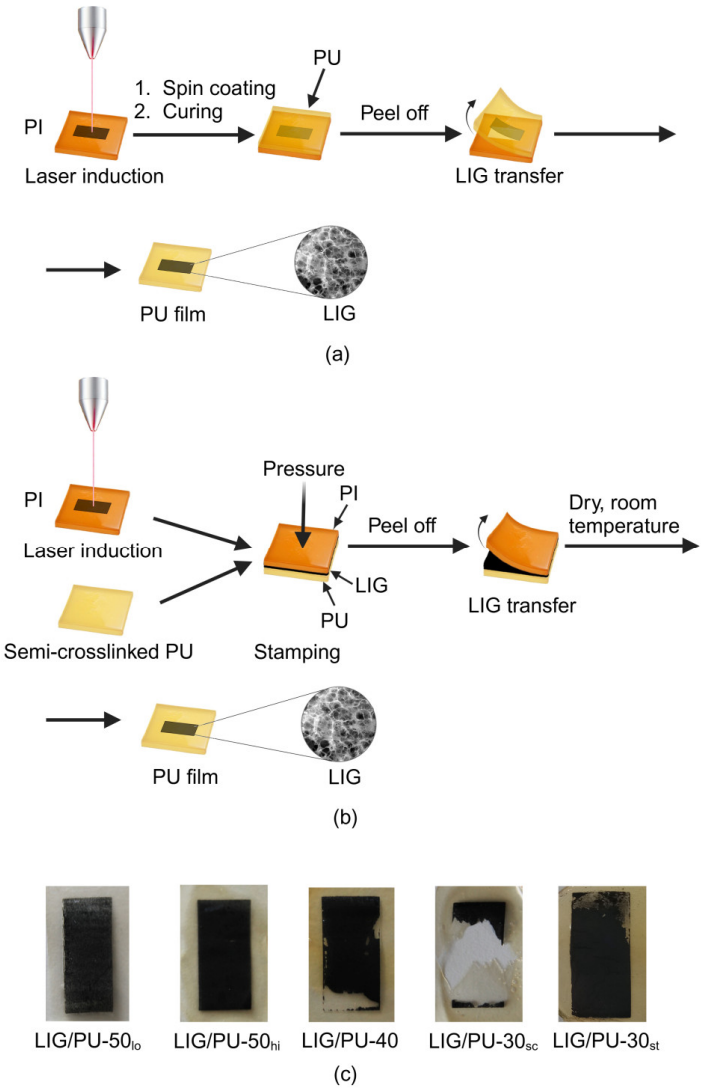

Figure 4. Schematic illustration of the LIG transfer using the following: (**a**) spin coating method, (**b**) stamping method, and (**c**) photographs of LIG/PU materials.

2.4. Methods of Characterization

The optical properties of the synthesized pure PU films, specifically PU-30, PU-40, and PU-50, were evaluated through UV-VIS spectroscopy using a Thermo Fisher Scientific EVO 60 spectrophotometer (Madison, WI, USA). The measurements were conducted in the wavelength range 200–1000 nm. Optical transmittance values at a wavelength of 500 nm were used to determine transparency.

The Fourier-transform infrared (FTIR) spectra of PU and LIG were recorded on a Nicolet 6700 spectrometer from Thermo Fisher Scientific (Waltham, MA, USA). For pure PU samples, spectra were acquired in non-destructive attenuated total reflection (ATR) mode. For LIG samples, the potassium bromide (KBr) pellet technique was employed. Powdered LIG samples were mixed with KBr and then pressed into pellets using a hydraulic press before being recorded. All spectra were collected in the mid-IR region (from 4000 to 400 cm^{-1}), with a resolution of 4 cm^{-1} and 32 scans for each sample.

Scanning electron microscopy (SEM) imaging of LIG/PU-50 cross-section and LIG surfaces, along with elemental composition analysis, was performed using a Phenom ProX microscope (Phenom, Eindhoven, The Netherlands) equipped with an energy-dispersive

X-ray spectrometer (EDX) without prior sample preparation. SEM micrographs of different magnifications (1000, 2000, 5000, and 10,000×) were obtained. The electron beam was accelerated using a voltage of 15 kV. LIG transferred onto PU films by spin coating was directly placed onto aluminum stubs for imaging.

Transmission electron micrographs of LIG (LIG/PU-50) were obtained using an FEI Talos F200X microscope (Thermo Fisher Scientific, Waltham, MA, USA) at an accelerating voltage of 200 kV. LIG was mechanically scratched from the PU-50 substrate, sonicated in ethanol, and the resulting suspension was deposited onto a TEM grid by drop casting.

Raman spectra of as-prepared LIG materials were recorded using a DXR Raman microscope (Thermo Fisher Scientific, Waltham, MA, USA) with a 532 nm excitation wavelength, a laser power of 2.0 mW, and an acquisition time of 10 × 10 s. Fluorescence in recorded spectra was automatically corrected using OMNIC software (Thermo Scientific), and baseline corrections were performed for all spectra. Raman spectroscopy, as a convenient method for the determination of crystalline sizes along an arbitrary axis of carbon materials, was used to obtain data for the intensity ratio $\frac{(I_D}{I_G)}$ of disordered (D) and graphitic peaks (G), to calculate crystalline sizes along the a-axis (L_a) for all the LIG materials. The following Equation (1) was used to calculate L_a (in nm) [64]:

$$L_a(\text{nm}) = (2.4 \times 10^{-10}) \times \lambda_{\text{laser}}^4 \times \left(\frac{I_G}{I_D}\right), \quad (1)$$

where λ_{laser} is the laser wavelength.

The X-ray diffraction (XRD) spectra of powdered LIG scraped from PI (~3.5 mg) and as-prepared LIG/PU films were investigated by means of a Riguku Ultima IV X-ray diffractometer (Tokyo, Japan) with Cu Kα radiation (1.54 Å). Diffraction patterns of LIG samples were collected in the range of 5–70° with a step size of 0.02°. The peaks in diffraction patterns were fitted by the Voigt deconvolution function, using the Peakfit program, resulting in the areas of peaks. The percent crystallinity was calculated by peak deconvolution and subsequent determination of the relative areas under the amorphous halo and the crystalline peaks of the X-ray diffraction pattern. The ratio of the area under the crystalline peaks to the total (amorphous + crystalline) area gave the degree of crystallinity [65]. The following Equation (2) was used for calculation of degree of crystallinity (W_c):

$$W_c = \frac{I_T - I_a}{I_T} \times 100\%, \quad (2)$$

where I_T is total intensity under the entire surface of the diffractogram, and I_a is sum of intensities originating from amorphous halos from PDMS and PU.

Nanoindentation measurements were conducted using a Nanoindenter G200 from Agilent Technologies (Santa Clara, CA, USA), equipped with a Berkovich diamond indenter tip from Micro Star Technologies (Huntsville, TX, USA). Before the indentation test, samples (3 mm × 3 mm) were glued to the holder. Measurements were taken at 25 points arranged in a 5 × 5 matrix on the composite surface, with a 100 μm distance between each measurement points. The maximum applied load was 30 mN, and the maximum indentation depth was 17 μm. A Poisson ratio of 0.49 was used for PU, as it is the dominant value compared to the LIG Poisson ratio (~0.17).

Tensile testing was performed at room temperature using a Universal Testing Machine (Shimadzu AGS-X, Tokyo, Japan) equipped with a 5 kN load cell. The machine resolution was ±0.5% (within 1/500 to 1/1 of load cell rated capacity), and crosshead position detection accuracy was 0.1%. The materials were prepared according to the ISO 527-1:2012 1BB standard and tested at a 3 mm/minute speed. All the materials were conditioned at

room temperature in a desiccator for 48 h before measurements. Three identical samples of each material were tested.

Adhesion between PUs and transferred LIG was checked using the Scotch tape test [49]. Adhesion was tested by using 50 mm thick adhesive tape (3M Deutschland GmbH, Neuss, Germany), and electrical resistance was measured using a digital multimeter (Sanwa Electric Instrument Co., Tokyo, Japan) before and after applying the adhesive tape to the LIG surface. The thickness of the PU substrates was measured using an Iskra NP37 (Iskra, Kranj, Slovenia) position indicator coupled with a stylus surface profilometer.

2.5. Cytotoxicity Assay

EA.hy926 cells (provided by Dr. Cora Jean Edgell, University of North Carolina USA) were cultured in Dulbecco's Modified Eagle Media supplemented with 10% fetal bovine serum, 2 mM L-glutamine, 100 mg/cm^3 streptomycin, 100 U/cm^3 penicillin, and 20% HAT media supplement. The culture was maintained in a humidified atmosphere containing 5% CO_2 at 37 °C and prepared for experiments using conventional trypsinization procedure.

To determine the percentage of cytotoxicity, the lactate dehydrogenase (LDH) release assay was performed. The EA.hy926 cells were seeded on sterilized PU-50 film (30,000 cells per well) and tested 48 h postseeding as previously described [45]. The percentage of cytotoxicity, measured by the LDH release assay, was expressed relative to positive control samples (cells grown without sample film, lysed with Triton X-100), taken as 100%.

2.6. Influence of Humidity on the Electrical Resistance

The change in electrical resistance was monitored at three different relative humidity levels (30, 60 and 90%), to investigate the influence of relative humidity (RH) on LIG. LIG/PI was fixed to the glass substrate and placed in the humidity test chamber (Environmental chamber—LIB TH-50B). Composites with attached copper contacts were connected to the Keithley 2450 for resistance monitoring at given humidity levels. Stabilization for each set of RH took 20 min at room temperature (25 °C).

2.7. Electrical Measurements and Pulse Monitoring

LIG/PU-based heterostructures were tested as pulse sensors. Conductive copper adhesive tapes were applied to the left and right edges of the LIG surface as electrical contacts to construct the electrical circuit, which was then connected to the measuring device. The Keithley 2450 (Solon, OH, USA) Source Measure Unit (SMU) instrument was used to measure real-time pulse signals of the LIG-based sensors attached to a pulse simulator mimicking human heartbeats. The BT-CEAB2 Pulse Assessment Simulator (BT Inc., Goyang, Republic of Korea) is a medical training device designed to simulate pulse palpation using an adult arm manikin. It generates pulses at the radial and brachial arteries, with an adjustable pulse rate range of 40–140 beats per minute (BPM) and three intensity levels. The skin of the simulator arm is made of a soft material resembling human skin. The sensor response to radial artery pulses (70 BPM; normal resting heart rate for adults) was recorded by applying a constant current of 0.1 mA and recording the voltage variation. Each sensor was tested five times to assess repeatability. This setup allowed us to eliminate artifacts from potential mechanical movements of the hand, ensuring accurate measurements. Additionally, using a simulator avoids the regulatory and ethical requirements associated with human subject testing.

We used "highpass" function in Python for baseline correction of pulse signals, according to Van Gent et al. [66]. Figure 5 illustrates the experimental setup, including the sensor attached to the pulse simulator and the data acquisition system.

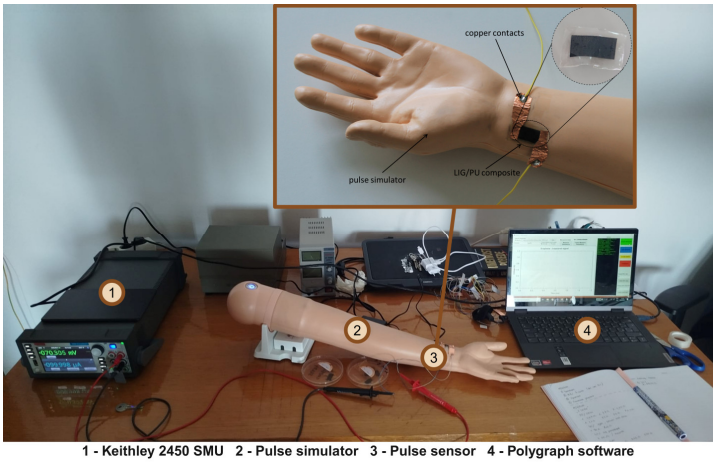

Figure 5. Photograph of the experimental setup with magnified part of the pulse simulator with attached LIG/PU-based sensor.

To facilitate reliable real-time measurements of the sensors, custom software was developed in Visual Studio for data acquisition and Keithley 2450 instrument control via GPIB commands. The software features a user interface that allows adjusting measurement parameters, such as the forcing current value, measurement duration, data formatting, and quality control of the conductive copper contacts with the sensor. The purpose of this custom software was to enable facile and reliable data collection for the measurements detailed in this paper.

3. Results and Discussion

Due to the structural characteristics of PUs, direct production of LIG on their surface was not feasible. Instead, LIG was transferred onto PU substrates using spin coating and stamping. The thin PU films with different wt.% of SSC were transparent, with transmittance >80% at a wavelength of 500 nm (Figure S1, Supplementary Materials).

The spin coating method enabled the successful transfer of LIG onto PU substrates with the highest soft segment content (PU-50) (Figure 4c). For PU-40, the transfer was partially successful, while for PU-30, the transfer was predominantly unsuccessful using the spin coating method, with LIG only adhering at the edges (Figure 4c). PUs with soft segment contents of 30, 40, and 50 wt.% were thin and flexible, while the samples containing 60 and 70 wt.% soft segments were brittle and mechanically unstable. For that reason, we did not use PU with 60 and 70 wt.% for LIG transfer in our study. LIG transfer onto PU-30 was feasible Via the stamping method.

Although the transfer quality for PU-30 (spin coating) and PU-40 substrates was sub-optimal, these samples were included in the characterization to provide a comprehensive understanding of how soft segment content affects the structure–property relationship and sensor performance. The results for PU-30 and PU-40 served as benchmarks, illustrating the limitations of substrates with lower SSC and emphasizing the superior performance of PU-50. These findings highlight the importance of optimizing SSC to achieve successful LIG transfer and reliable wearable device performance. By including these suboptimal samples, this study provides valuable guidance for future material design and optimization. Despite the poor transfer quality observed for PU-30 and the partially successful transfer for PU-40, these samples were characterized to systematically analyze the influence of substrate properties on LIG transfer and performance. This approach allowed us to identify PU-50 as the optimal substrate for wearable pulse sensors.

3.1. FTIR Spectra Analysis

FTIR analysis was performed to confirm the chemical structure of the synthesized PU substrates, and to identify functional groups present on the LIG surface. The characteristic stretching and deformation vibrations of functional groups in the FTIR spectra of LIG and PUs are indicated in the spectra shown in Figure 6.

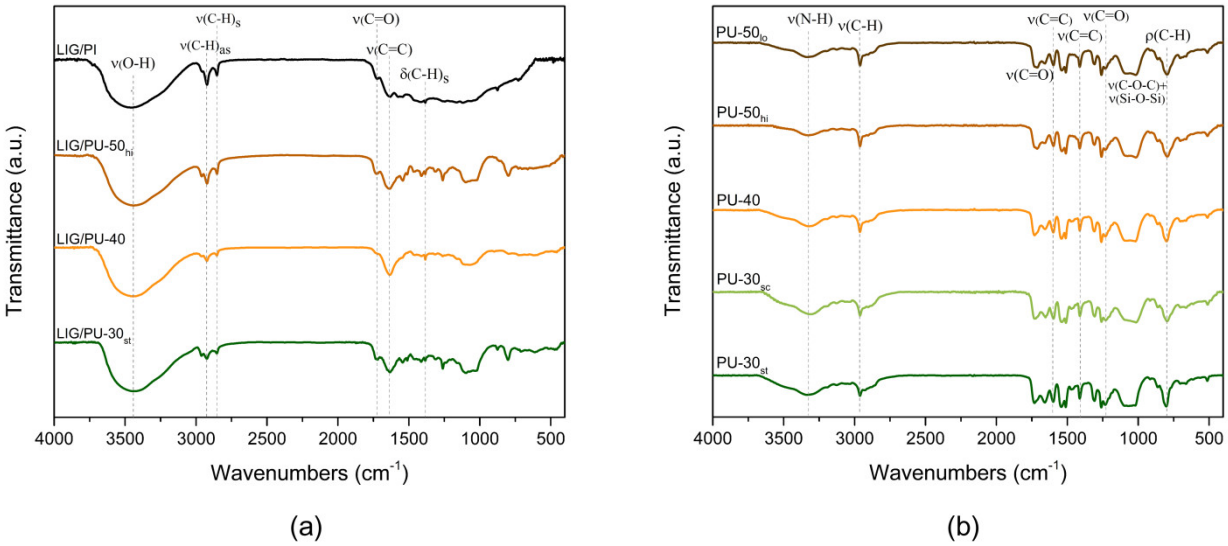

Figure 6. The FTIR spectra of (**a**) LIG scraped off from different polymeric substrates and (**b**) PUs with different wt.% of SSC. Stretching vibrations are denoted as ν, valence or deformation vibrations as δ, and rocking vibrations as *ρ*. Gray dashed lines indicate the positions of characteristic vibrations in FTIR spectra.

In the spectra of all LIG samples, absorption bands were observed at approximately 3450, 2925, 1725, 1630, 1385, and 875 cm^{-1}. The broad band at ~3450 cm^{-1} corresponds to O–H stretching vibrations, and its intensity possibly arises from water absorbed by potassium-bromide during pellet preparation [67]. The bands at ~2925 cm^{-1} and ~1725 cm^{-1} correspond to asymmetric and symmetric stretching vibrations of C–H and C=O groups, respectively. Skeletal vibrations of C=C bonds in the aromatic structure were observed at ~1630 cm^{-1}. The band at ~1385 cm^{-1} corresponds to C–H bending vibrations, while the peak at 875 cm^{-1} is associated with C-H rocking vibrations [68–70].

The typical bands related to the polyurethane structure were observed in the FTIR spectra of PUs (Table 1) [46]. The complete consumption of isocyanate groups is proved by the absence of NCO stretching vibrations at around 2270 cm^{-1} in all materials.

Table 1. Summary of the assignment and position of bands in the FTIR spectra of PUs with different wt.% of the soft segments.

Vibration Mode	Wavenumbers (cm^{-1})
ν(N–H)	3328
ν(C–H)	2962
ν(C=O)	1700–1711
ν(C=C) (from aromatic ring)	1598 and 1413
ν(C–N) + δ(N–H) (amide II and amide III)	1539 and 1308
$\nu(C–O)_s$ and $\nu(C–O)_{as}$ from ester	1232 and 1259
ν(C–O–C) + ν(Si–O–Si)	1018, 1090
ρ(C–H) from $SiCH_3$	797

3.2. Scanning Electron Microscopy

SEM was conducted to investigate the morphology of LIG. As can be seen, SEM micrographs of LIG/PU materials transferred via spin coating (Figure 7) revealed a hierarchical porous structure with interconnected pores and graphene located on the walls of the formed pores. This sponge-like open pore morphology of the LIG surface is consistent with typical porous LIG structures reported in the literature [39].

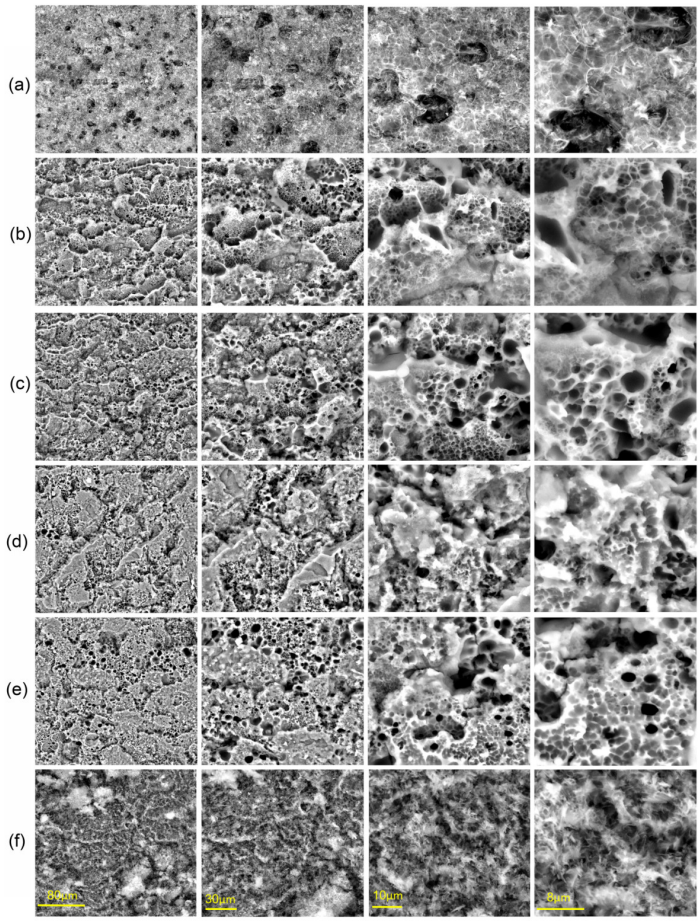

Figure 7. SEM micrographs of LIG samples: (**a**) LIG/PI, (**b**) LIG/PU-50$_{lo}$, (**c**) LIG/PU-50$_{hi}$, (**d**) LIG/PU-40, (**e**) LIG/PU-30$_{sc}$, and (**f**) LIG/PU-30st at different magnifications (1000×, 2000×, 5000× and 10,000×, from the left to the right).

Using ImagePro Plus software, the lateral dimensions of surface-accessible macropores were estimated from SEM micrographs. For each material, we used ten arbitrary pores to determine the average pore diameter. The average pore diameter was in the range between 1.3 and 3 µm for LIG transferred via spin coating. Notably, LIG/PU-30$_{sc}$ exhibited larger average pore diameters (1.8 ± 0.8 µm) compared to LIG/PU-30st (0.8 ± 0.1 µm), highlighting differences between the spin coating and stamping methods. The pores on the surface of LIG that was transferred via stamping were smaller, likely due to the mechanical pressure that was applied during transfer.

Additionally, the thickness of the LIG transferred onto the PU-50 substrate was estimated at approximately 10 µm based on the cross-sectional SEM image (Figure S2, Supplementary Materials), in agreement with values reported for LIG directly produced on a PI substrate [14]. However, due to the porous nature of the material, thickness was not uniform across the entire surface.

EDX mapping was performed to determine the atomic concentration of different elements and their distribution across the surface of the transferred LIG. The results from

EDX analysis (Figure 8 and Table S1, Supplementary Materials) showed a high carbon concentration in LIG, but a lower atomic percentage of carbon compared to directly induced graphene on PI [14]. The carbon content is >60 at. % for all transferred LIG materials, with a maximum of ~69 at. % in LIG/PU-50. Oxygen content ranged from ~17 at. % to ~23 at. %, attributed to partial oxidation of LIG in air. Nitrogen content, associated with urethane groups in the PU structure, increased slightly with higher hard segment content in the PUs. PDMS is known to have lower surface energy than polyurethane [71], and the presence of silicon in transferred LIG materials was due to the migration of PDMS to the PU surface and, subsequently, to the LIG surface. PU-30 has a smaller wt.% of PDMS macrodiol and lower at. % of silicon in the structure, resulting in lower silicon concentrations in the corresponding LIG sample.

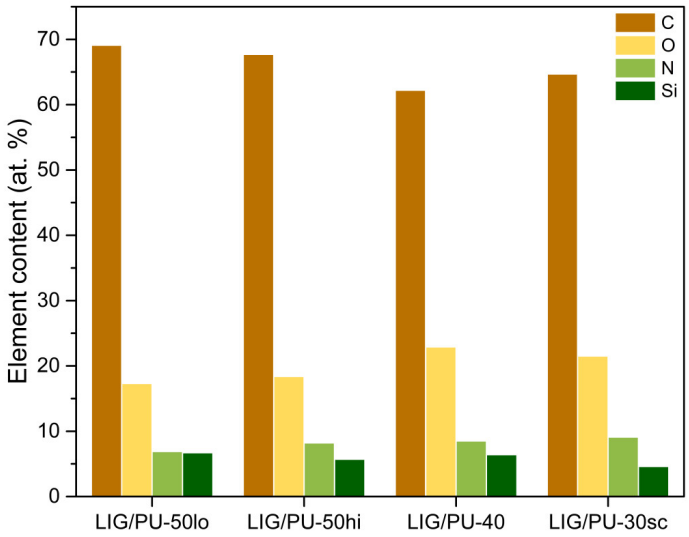

Figure 8. Graphical representation of element composition obtained from EDX analysis of LIG surface transferred to PUs via the spin coating method.

3.3. Raman Spectroscopy

Raman spectroscopy was used to confirm the presence of graphitic material and to assess the quality of LIG samples. Raman spectra for LIG samples on different substrates are shown stacked in Figure 9.

LIG materials exhibited typical Raman spectra with the D peak at ~1360 cm^{-1}, induced by sp^2 carbon atoms breathing vibrations in aromatic rings or induced by defects (A_{1g} symmetry mode); the G peak at ~1590 cm^{-1}, which arises from stretching vibrations of sp^2 carbon atoms (E_{2g} symmetry mode) and the 2D peak at ~2700 cm^{-1} as a second-order mode of the D peak (Tables S2 and S3, Supplementary Materials). Raman shifts for the most prominent peaks in LIG were consistent with values reported in the literature [8]. LIG transferred via spin coating exhibited visually similar Raman spectra with well-defined 2D peaks (Figure 9). However, the spectrum of LIG transferred via stamping (LIG/PU-30st) contained broad, poorly defined peaks indicative of an amorphous nature [72]. The 2D band in this material was broad with low intensity, resembling the spectrum of reduced-graphene oxide, similar to the Raman spectra of LIG transferred to SEBS [16] and PLA [56].

Peak deconvolution was performed to determine the positions of characteristic bands, the intensity of peaks, the value of I_D/I_G, and the full width at half maximum (FWHM) of the D, G, and 2D bands (Table S4, Supplementary Materials). The software PeakFit (v4.12) was used for deconvolution of each peak in the range 1200 to 1700 cm^{-1}, and in the range 2000 to 3000 cm^{-1} (Figures S3 and S4, Supplementary Materials). Intensities were defined

as integrated areas under the peaks (in %). D'', D*, 2D, and D + G peaks were fitted to the Gauss function, and D, G, and D' peaks were fitted to the Voigt function [31,73].

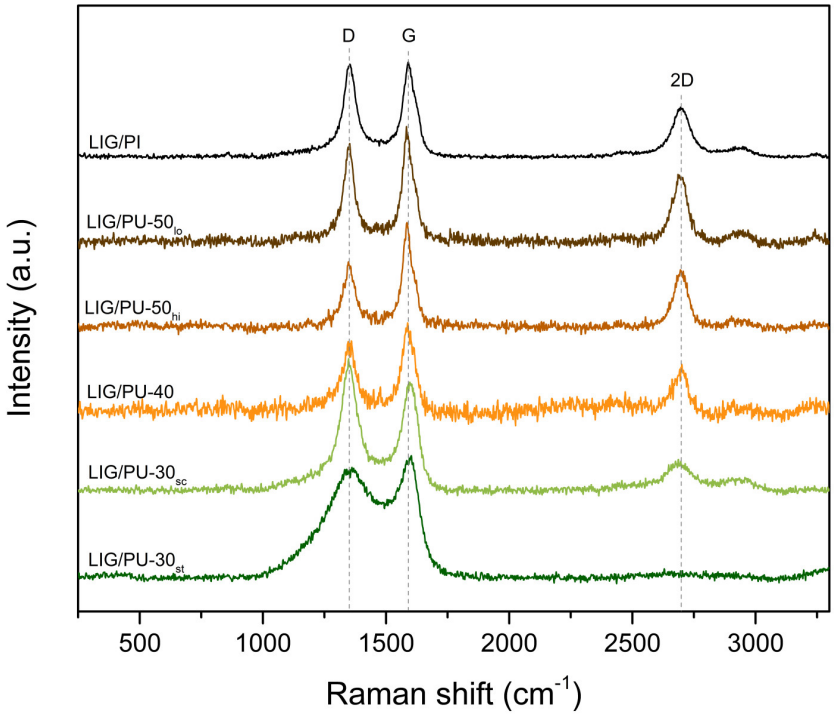

Figure 9. The Raman spectra at higher quality positions of LIG samples transferred on PUs with varying content of soft segments. LIG/PI is given for comparison. Gray dashed lines indicate the positions of marked bands.

The presence of defect-activated peaks (D, D', and D + G bands) in the Raman spectra confirmed the defective nature of LIG. The I_D/I_G ratio from Raman spectra is usually used as a quantitative measure of disorder in graphitic materials [74]. As shown in Figure 10a (darker shade), the material with the lowest I_D/I_G (~0.7) was LIG transferred onto PU-50. Such a value for the ratio of intensities of the D and G peaks corresponds to a crystallite size (L_a) of ~28.5 nm, which corresponds to a small concentration of defects. In contrast, LIG transferred onto PU-30 (via spin coating and stamping) exhibited the highest degree of disorder, with L_a ~14.4 nm and ~16.9 nm, respectively. LIG transferred onto PU-30 has a higher defect density, with $I_D/I_G > 1$. A general trend was observed: as SSC in PU increased, D band intensity, and consequently I_D/I_G decreased, indicating improved structural quality in LIG transferred onto substrates with higher SSC. Transfer of LIG onto substrates with 30 and 40 wt.% of SSC was partial using the spin coating method (see Figure 4c), which can be related to better adhesion between LIG and PI compared to adhesion between LIG and PUs with a higher wt.% of polar hard segments [75] in the polymeric matrix. These considerations suggest that LIG/PU-50 is structurally the highest quality material between the synthesized PUs.

The number of graphene layers could be estimated from the shape and FWHM of the 2D band, for fewer graphene layers (up to seven) [76], and based on the intensity of the 2D peak compared to the G peak intensity. Single-layer graphene exhibits a sharp, high-intensity 2D peak [77], whereas a 2D band with reduced intensity is an indication of a few-layer graphene. According to the literature [12,78], the value of the I_{2D}/I_G can be correlated to a specific number of graphene layers. Generally, a lower ratio of intensities of the 2D band to the G band suggests the presence of a higher number of layers. The I_{2D}/I_G ratio for all LIG samples was <1 (Figure 10a, lighter shade), suggesting the presence of a few-layer graphene consistent with TEM observations (see below). LIG/PU-50 exhibited a

narrower 2D band (FWHM ~70 cm^{-1}) than LIG/PU-40, LIG/PU-30_{sc}, and LIG/PU-30st (FWHM ~80 cm^{-1}), indicating higher crystallinity, fewer defects, and better LIG quality [79] (Table S4 and Figure S5, Supplementary Materials).

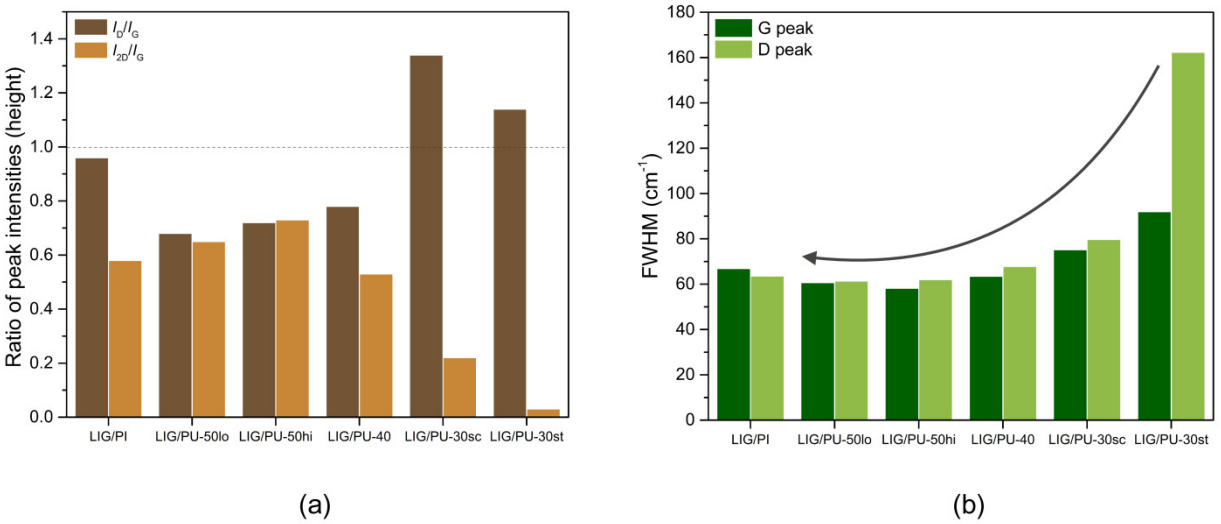

Figure 10. Data obtained from analysis of Raman spectra of LIG on different substrates: (**a**) intensity ratio of D and G peaks (darker shade), intensity ratio of 2D and G peaks (lighter shade). The dashed line emphasizes low defect concentration ($I_D/I_G < 1$) and the multilayered structure of the LIG ($I_{2D}/I_G < 1$). (**b**) FWHM for the G peak (darker shade) and the D peak (lighter shade). The arrow points in the direction of the reduction in the FWHM of the D and G peaks as the SSC increases.

The FWHM of the G and D bands (Figure 10b) was smaller for LIG transferred onto substrates with higher SSC, particularly PU-50. The reduced FWHM values of these bands are indicative of higher crystallinity and structural integrity of LIG [80].

Additionally, EDX showed slightly higher oxygen content in the LIG transferred to the PU-30 via spin coating, likely due to the presence of more oxygen-containing functional groups, which were also confirmed by FTIR. These functional groups may act as defects [81] and influence the polarity of LIG on these substrates. Partial oxidation of LIG in air likely contributed to the observed oxygen content in the LIG samples.

All aforementioned parameters extracted from Raman analysis indicate that LIG transferred onto PU-50 substrates Via spin coating exhibited the highest-quality among the investigated samples.

3.4. Transmission Electron Microscopy

High-resolution TEM (HR-TEM) was employed to analyze the structure and interplanar distances in few-layer graphene. According to data obtained from Raman spectroscopy, LIG/PU-50_{lo} showed the highest structural quality among the investigated materials and was chosen for the TEM analysis. TEM micrographs (Figures 11 and S6, Supplementary Materials) of LIG scraped off the PU-50_{lo} substrate revealed ordered domains, in addition to noticeable disordered, randomly oriented layers. Interplanar spacing between graphene sheets was determined from ordered domains and shows non-uniform values (0.34–0.37 nm) within different domains. Interlayer spacings near 0.34 nm agree with values reported in the literature for LIG [8]. Larger interlayer spacings (>0.34 nm) are attributed to oxygen functional groups intercalated within graphene layers [69,82], a finding corroborated by EDX analysis, which indicated relatively high oxygen content in the LIG/PU-50 material.

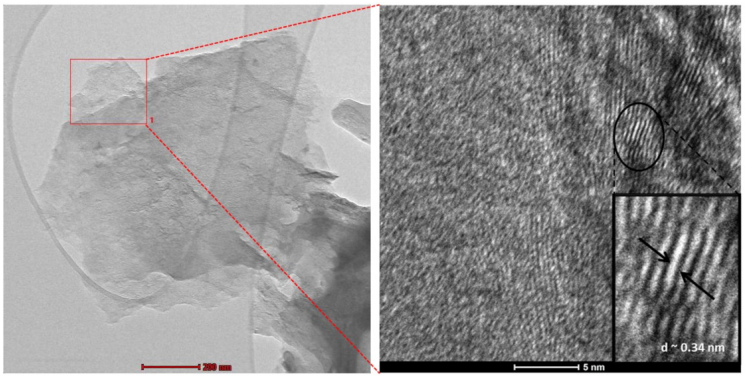

Figure 11. (**a**) TEM and (**b**) HRTEM micrographs of LIG.

3.5. X-Ray Diffraction

The crystalline structure of LIG/PU and LIG/PI materials was analyzed using XRD. XRD patterns of LIG/PU are depicted in Figures 12 and S7 in Supplementary Materials. The results of XRD analysis are given in Table 2.

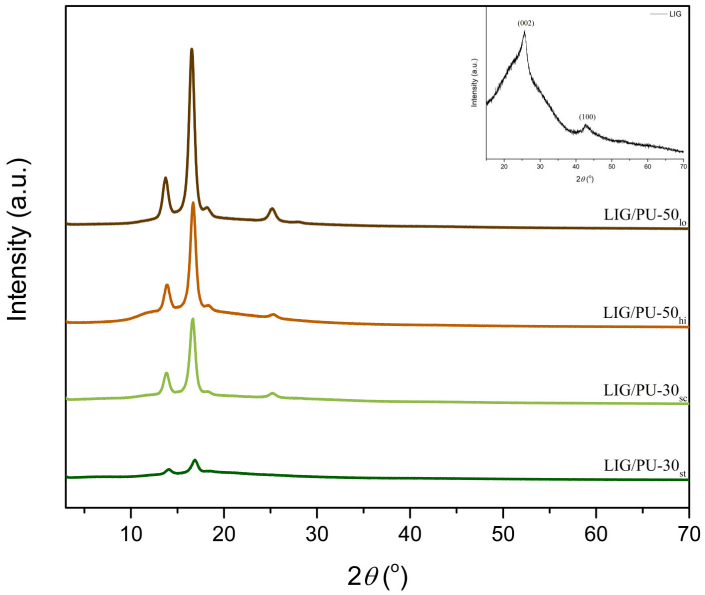

Figure 12. The XRD patterns of selected LIG/PU composites. Inset: XRD pattern of powdered LIG.

Table 2. Positions of diffraction maxima obtained by deconvolution of XRD patterns and the degree of crystallinity of LIG/PU films.

Material	Amorphous Halo of PDMS	Crystalline Peak of PU	Amorphous Halo of PU	Crystalline Peak of LIG (002)	Degree of Crystallinity (W_c)
	2θ (°)	2θ (°)	2θ (°)	2θ (°)	%
LIG/PU-50$_{lo}$	13.92	16.56	18.4	24.95	42.6
LIG/PU-50$_{hi}$	13.83	16.52	18.6	25.04	38.8
LIG/PU-30$_{sc}$	13.92	16.61	19.9	24.98	34.8
LIG/PU-30st	14.13	16.84	18.4	24.46	26.8

Characteristic reflections from the crystalline phase of LIG in LIG/PI were observed at 2θ ~25° and ~43°, corresponding to the (002) graphitic plane and (100) turbostratic carbon plane, respectively [23]. These observations are consistent with literature data [83].

The peak at 2θ ~25° confirms the highly crystalline structure of the graphene sheets in LIG/PI [83].

The XRD patterns of all LIG samples transferred to PU substrates showed a peak at ~25°. Notably, LIG transferred to PU with 50 wt.% SSC exhibits a more pronounced peak than the LIG transferred to PU with 30 wt.% SSC, which is another indicator that higher contents of the soft segment are favorable for LIG transfer. However, this peak for LIG/PU-30st showed significantly lower intensity (Figure S7, Supplementary Materials) compared to LIG/PU-30_{sc} and other LIG-based materials, indicating a more amorphous graphene structure, consistent with Raman spectroscopy results.

The inter-planar distance (d) was calculated using Bragg's equation, $n\lambda = 2d\sin\theta$. For the first diffraction order (n = 1), x-ray wavelength of 1.54056 Å, and a 2θ angle of 25°, the calculated value of the van der Waals inter-planar distance between (002) planes was 3.5 Å, which is in accordance with the literature data for LIG [8,84]. This value aligns within the error range of ~3.4 Å obtained Via TEM analysis of LIG/PU and is attributed to defect regions within the hexagonal graphene layers [8].

Due to the phase separation between PDMS and MDI–HBP segments, the XRD patterns of PU materials have distinct peaks associated with these phases. The primary crystalline peak at 2θ ~17° originates from the hard segment (urethane) components, reflecting an ordered structure arising from hydrogen bonding [85]. Broader, less intense peaks at ~14° and ~19° correspond to the amorphous halos of the PDMS phase and PU, respectively. These results confirm that PDMS blocks form distinct, separated phases at room temperature.

Degree of Crystallinity

The degree of crystallinity was quantified for the LIG/PU films based on the XRD diffractograms. As shown in Figure 12, the peak intensities varied across the samples, indicating differences in crystallinity. The degree of crystallinity of the PUs ranged from ~27 to ~43% (Table 2) and increased with higher soft segment content. A noticeable increase in the intensity of the PU crystalline peak (2θ ~17°) was observed with increasing crystallinity. Conversely, a reduction in crystallinity was observed in PUs with higher urethane content (lower SSC), attributed to restrictions imposed by covalent linkages and strong interchain interactions mediated by hydrogen bonding.

3.6. The Nanoindentation Results

Nanoindentation is an advanced technique employed to characterize the mechanical properties of the outermost surface layers, offering significant advantages over classical tensile testing methods. Table 3 summarizes the mechanical properties, including the average values of the modulus of elasticity (Young's modulus), hardness, and plasticity, for LIG/PU and LIG/PI materials. Representative indentation load–displacement curves for LIG/PU materials with varying soft segment content are depicted in Figure S8 (Supplementary Materials).

Table 3. Nanomechanical properties of LIG/PU and LIG/PI materials.

Material	Young's Modulus (GPa)	Hardness (GPa)	Plasticity (Ductility) Index
LIG/PU-50_{lo}	0.5 ± 0.3	0.014 ± 0.009	38.79
LIG/PU-50_{hi}	0.06 ± 0.05	0.009 ± 0.005	7.22
LIG/PU-40	1.0 ± 0.3	0.05 ± 0.02	20.90
LIG/PU-30_{sc}	1.4 ± 0.5	0.03 ± 0.02	43.24
LIG/PU-30st	0.5 ± 0.2	0.008 ± 0.004	56.63
LIG/PI	0.3 ± 0.1	0.005 ± 0.002	60.00

Hardness is a measure of a material's resistance to localized surface deformation, while the elastic modulus quantifies the overall stiffness of the polymer network. Both hardness and stiffness (as characterized by Young's modulus) were observed to increase with a reduction in soft segment content in PU. These findings are consistent with previous studies, which have established that chain flexibility and cross-linking density significantly influence the hardness of polymeric materials [86]. The cross-linking density was found to increase as the soft segment content decreased. Conversely, a higher content of PDMS soft segments in the PU structure results in softer films (lower modulus) and capable of reaching larger deformations (lower hardness) [87]. The elastic modulus of LIG/PU materials ranged from 0.5 GPa to 1.4 GPa (except for LIG/PU-50_{hi}), while pure PU exhibited a lower value of approximately 0.27 GPa. LIG/PI had a modulus of 0.3 GPa, comparable to pure PU. Among the LIG/PU materials, LIG/PU-50_{lo}, LIG/PU-40, and LIG/PU-30_{sc} exhibited higher Young's modulus and hardness values compared to LIG/PI. LIG/PU-50_{lo} and LIG/PU-50_{hi}, with lower moduli of 0.5 ± 0.3 GPa and 0.06 ± 0.05 GPa, respectively, demonstrated that film thickness has a significant influence on stiffness, with thinner films showing better mechanical performance. Among the LIG-based materials with 30 wt.% soft segment content, LIG/PU-30_{sc} surpasses LIG/PU-30st in terms of stiffness and hardness, further underscoring the critical role of the preparation method in tailoring material properties for specific applications.

The ratio of Young's modulus to hardness, often referred to as the plasticity or ductility index, reflects the relative contribution of plastic deformation during indentation [88]. This index also correlates with fracture toughness [89]. Among the LIG/PU materials, LIG/PU-50_{lo}, LIG/PU-30_{sc}, and LIG/PU-30st exhibited the highest plasticity indices, indicating superior fracture toughness. However, all LIG/PU materials demonstrated lower plasticity and fracture toughness compared to LIG/PI.

Compared to LIG/PU-50_{hi}, which has a lower modulus and plasticity index, LIG/PU-50_{lo} demonstrates a better combination of mechanical properties, making it a most suitable candidate as an advanced material for wearable applications.

3.7. Tensile Testing

The mechanical properties of the synthesized pure PU films, specifically PU-30, PU-40, and PU-50, were evaluated through tensile testing, with the corresponding stress–strain curves presented in Figure 13 and the key mechanical parameters summarized in Table 4.

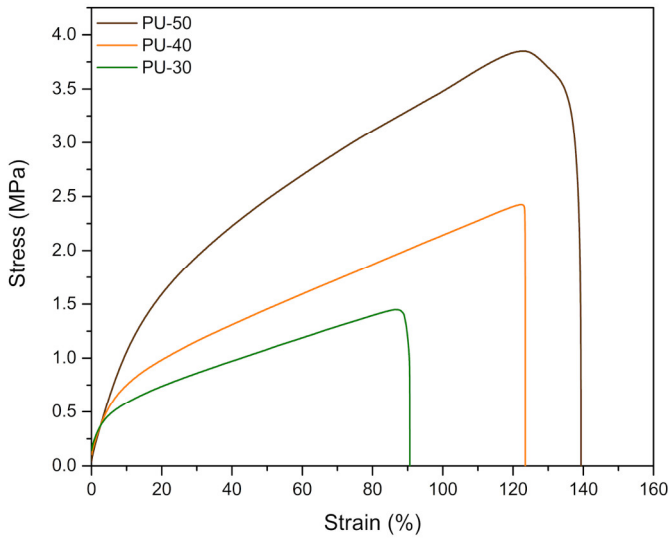

Figure 13. Stress–strain curves of pure polyurethanes with 30, 40, and 50 wt.% of soft segment content.

Table 4. Mechanical properties of pure PU-30, PU-40, and PU-50 films.

Pure PUs	Tensile Strength (MPa)	Elongation at Break (%)	Young's Modulus (MPa)
PU-30	1.45	90.62	11.21
PU-40	2.43	123.40	14.33
PU-50	3.85	139.25	22.32

The obtained results demonstrate a clear correlation between the SSC and the overall mechanical performance of the PUs, where an increase in SSC leads to notable improvements in tensile strength, elasticity, and flexibility. The tensile strength of the PUs increased from 1.45 MPa for PU-30 to 3.85 MPa for PU-50, representing an enhancement of over 165%, while Young's modulus exhibited a significant rise from 11.21 MPa to 22.32 MPa, indicating increased stiffness. Simultaneously, elongation at break improved from 90.62% to 139.25%, highlighting the enhanced stretchability of the PU films with higher SSC, which is critical for applications requiring flexible and durable polymeric materials.

This observed mechanical behavior can be attributed to the increased content of PDMS soft segments within the polymer matrix, which enhances chain mobility and elasticity, allowing the material to undergo larger deformations before failure. As the SSC increases, the polymer structure becomes more flexible, reducing rigidity and leading to higher elongation at break values. Interestingly, despite the significant increase in tensile strength and Young's modulus, PU-50 maintains excellent elasticity, as reflected in its highest elongation at break, suggesting that the polymer achieves an optimal combination of strength, stiffness, and flexibility.

The observed trends confirm that fine-tuning the SSC allows for precise control over the mechanical properties of PUs, enabling their use in a wide range of engineering, biomedical, and flexible electronic applications. The results of this study emphasize the crucial role of polymer composition in determining mechanical behavior, reinforcing the versatility of PU films in next-generation soft electronics and biomedical devices.

3.8. Adhesion Testing Via the Scotch-Tape Method

Scotch tape tests were applied on selected materials (LIG/PI, LIG/PU-30st, LIG/PU-40, and LIG/PU-50) to investigate the adhesion between LIG and different substrates (Figure S9, Supplementary Materials). The results revealed a significant variation in adhesion depending on the substrate type. The electrical resistance was measured before and after applying the adhesive tape to the LIG to determine the change in resistance (in %). Adhesive tape was applied to the surface of the LIG/substrate using manual pressure.

The electrical resistance of LIG/PI increased by more than 400%, rising from ~400 Ω to ~2 kΩ after tape removal, indicating extremely weak adhesion between LIG and the commercial PI substrate. A similar trend was observed with LIG/PU-30st, where the resistance increased by approximately 375% (from 2.1 kΩ before to 10 kΩ after the tape test). In contrast, LIG transferred onto PU-40 exhibited a resistance increase of approximately 110%, from 2.1 kΩ to 4.4 kΩ, suggesting improved, but still suboptimal adhesion. The strongest adhesion was observed for LIG/PU-50, where the resistance increased by less than 30%, from 6.6 kΩ to 8.5 kΩ, demonstrating significantly enhanced interfacial bonding between LIG and the PU matrix.

The chemical composition and surface properties of the substrate play a crucial role in LIG-substrate interactions. PU substrates contain urethane (—NHCOO—) functional groups that facilitate hydrogen bonding and dipole interactions, contributing to stronger interfacial adhesion. The degree of phase separation between soft and hard segments in PU also influences adhesion performance. Higher SSC, as in PU-50, enhances flexibility and elasticity, allowing the polymer matrix to better conform to the porous structure of LIG,

thereby improving mechanical stability and adhesion. The Scotch tape test revealed that although the transfer Via spin coating increases the electrical resistance of LIG, it improves the adhesion between LIG and the substrate. These findings underscore the importance of optimizing the SSC in PU substrates to achieve strong adhesion, which is critical for the durability and stability of wearable sensors.

3.9. Cytotoxicity

Endothelial cells, which comprise the continuous inner lining of the cardiovascular system, are regularly used as a model for assessing the biocompatibility of different materials [90]. The results of the LDH test showed that PU-50 was not cytotoxic (Figure 14). Namely, the LDH release was less than 5% (as compared to Triton X100), indicating the absence of cell membrane damage in cells growing on the investigated material, 48 h post-seeding.

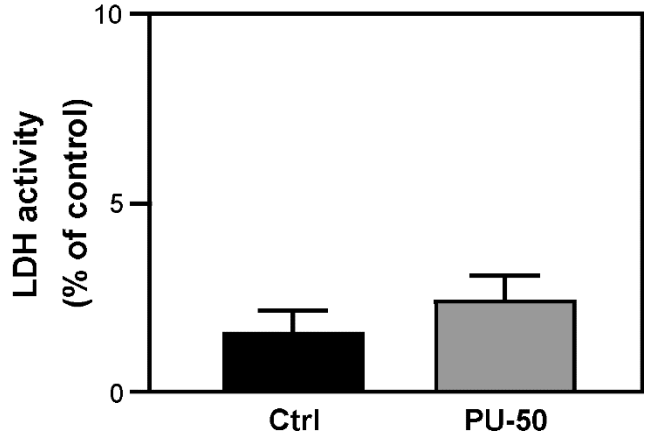

Figure 14. Influence of PU-50 film on LDH release in EA.hy926 cell line after 48 h (Ctrl—control).

3.10. Influence of Humidity on LIG

To evaluate the sensor cross-sensitivity to humidity, we measured the electrical resistance of LIG at relative humidity (RH) levels of 30%, 60%, and 90% [91]. The obtained results indicate that at 30% RH, the electrical resistance was 2078.0 ± 0.1 Ω, while at 60% RH, it increased slightly to 2078.5 ± 0.1 Ω, and at 90% RH, it reached 2079.2 ± 0.2 Ω. These minimal resistance variations suggest that LIG-based sensors have minimal cross-sensitivity to humidity.

3.11. Pulse Sensing Application

In the field of wearable healthcare systems, detecting the human pulse is an essential feat. LIG transferred onto synthesized biocompatible cross-linked PU substrates has not been used as a pulse sensor, even though prospects for the use of this material for this application are apparent due to the excellent sensing performance of LIG and biocompatibility and versatility of PU.

Herein, LIG serves as the active surface of the sensor, while the PU film acts as a flexible and biocompatible substrate. The piezoresistive properties of LIG enabled the detection of periodic voltage variations corresponding to mechanical pulse signals generated by a pulse simulator to which the sensor was attached. The simulator was used instead of a real person to ensure consistent and repeatable conditions, eliminate variability in human subjects, and allow safe, controlled training.

The working principle of the LIG/PU-based pulse sensor relies on the piezoresistive effect, where mechanical deformation alters the electrical resistance of the conductive LIG. When the sensor is placed on the pulse simulator and subjected to periodic pulse waves,

the flexible polyurethane substrate undergoes slight deformations. These deformations induce strain in the LIG layer on the surface of the PU substrate, which leads to measurable resistance variations due to strain in the graphene lattice. This resistance change is proportional to the applied deformation and can be measured in real time.

To assess repeatability, real-time data were collected over several minutes in five separate experiments for each selected sensor, based on the following materials: LIG/PU-50_{lo}, LIG/PU-50_{hi}, LIG/PU-40 and LIG/PI (Figures 15 and S10–S13, Supplementary Materials). The transfer of LIG to PU-30 Via spin coating was unsuccessful, so this composite was excluded from the measurements. The LIG/PU-50 sensor exhibited the best performance, prompting us to investigate the influence of substrate thickness by testing two different thicknesses. Similarly, data from a LIG/PI-based sensor were collected for comparison, and the PI used in this experiment had the same thickness as PU-50, within experimental error. The thicknesses of the synthesized PU films and the LIG electrical resistance after making electrical contacts are provided in Table 5.

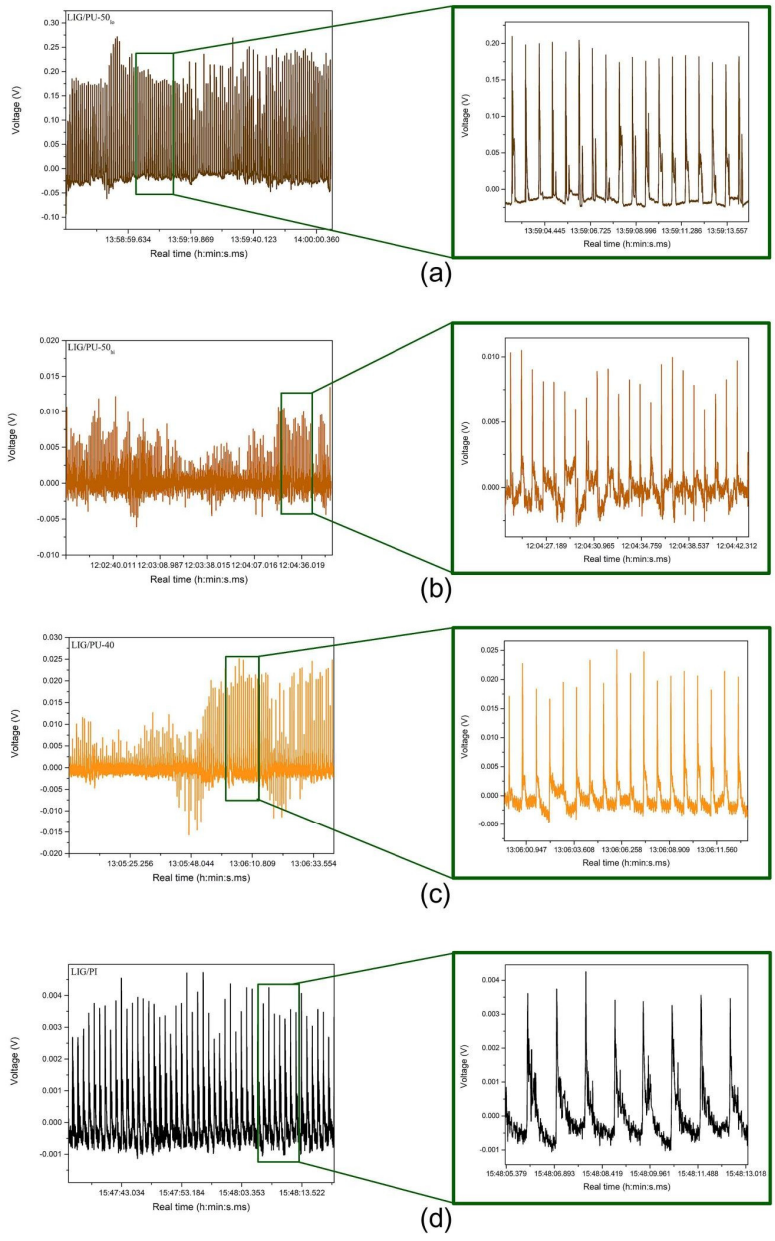

Figure 15. Pulse sensing with LIG-based sensors (**a**) LIG/PU-50_{lo}, (**b**) LIG/PU-50_{hi}, (**c**) LIG/PU-40, and (**d**) LIG/PI: voltage variation in real-time.

Table 5. The thicknesses of the synthesized PUs and commercial PI with the electrical resistance of LIG transferred on PUs and directly produced on PI.

Material	Thickness (μm)	LIG Electrical Resistance (kΩ)
PU_{lo}-50	77	11.0
PU_{hi}-50	88	4.8
PU-40	100	9.5
PI	76	1.2

Figure 15 depicts examples of the pulse signal obtained for each sensor. The results were obtained from the pulse simulator instead of a real human wrist. All data are presented with a part of the signal magnified to clearly show the pulses. The data have been corrected for baseline drift by applying a high pass filter in postprocessing.

The signal-to-noise ratios for measurements presented in Figure 15 were calculated as the maximum peak height divided by the standard deviation of the baseline [92]. The calculated SNR ratios for LIG on different substrates are as follows: $(SNR)_{PU\text{-}50lo}$ = 270, $(SNR)_{PU\text{-}50hi}$ = 17, $(SNR)_{PI}$ = 13, and $(SNR)_{PU\text{-}40}$ = 10.

The electrical resistance of the LIG/$PU\text{-}50_{lo}$ was 11 kΩ, with a modulus of elasticity obtained from nanoindentation measurements of approximately 0.5 GPa. In contrast, the electrical resistance of LIG/PI was measured to be 1.16 kΩ, with a modulus of elasticity near 0.3 GPa. The sensor based on LIG/$PU\text{-}50_{lo}$ had significantly greater SNR compared to the sensor based on LIG/PI. A higher heartbeat sensing quality with sensors that have lower stiffness has been observed before with LIG-based sensors on PDMS [14]. The enhanced sensitivity to small deformations from simulated heartbeats could also occur due to the reduced thickness of the substrate [5,12] and the structure of PUs with 50 wt.% SSC, which affects the mechanical properties of the composite.

Adjusting SSC enables tuning the mechanical and physicochemical properties of polyurethane substrates. Higher SSC enhances flexibility and good adhesion, which are critical for achieving consistent LIG transfer and optimal sensor performance. In this study, polyurethane with 50 wt.% SSC (PU-50) demonstrated superior mechanical properties and achieved the highest SNR (270) among tested sensors, attributed to improved LIG adhesion and reduced defect density.

The dimensions and morphology of laser-induced graphene (LIG) pores directly influence its electrical resistance and, consequently, its overall electrical performance when applied as a piezoresistive sensor [8]. The interconnected porous network facilitates strain-induced variations in electrical resistance by enabling the deformation of the LIG network during mechanical loading. This feature contributes to the high sensitivity of LIG-based sensors, particularly in detecting subtle pulse signals [8]. FTIR (Figure 6) data highlight the presence of oxygen-containing functional groups in LIG, such as C–O and C=O, which influence the adhesion of LIG to the PU substrate. Strong adhesion ensures mechanical integrity during deformation, directly impacting the stability and repeatability of the sensor signal. The chemical structure of PU, particularly the ratio of soft and hard segments, affects the flexibility and elasticity of the substrate. Substrates with higher soft segment content (e.g., PU-50) exhibit lower stiffness, enabling better deformation sensing by the LIG layer, thereby enhancing the sensor's piezoresistive response. These findings demonstrate that optimizing both topography and chemical bonding is critical to achieving good sensing performance, with PU-50 providing the best combination of mechanical and structural properties for pulse sensing applications.

Based on the obtained SNRs, LIG transferred onto the thin PU-50 film emerges as the most promising sensing substrate in this study, showing the highest signal-to-noise ratio. This sensor, based on LIG/PU, could be applied as a skin-safe, wearable, flexible

patch. Moreover, these biocompatible, non-toxic, and flexible sensors are not limited to single-use applications. These findings suggest that LIG/PU-based devices can serve as effective, biocompatible, and biostable alternatives in biomedical sensing technologies for long-term use, including in the wearable medical and sports industries. The robustness of the sensors during transfer, as well as their excellent elasticity, hint at a potentially long useful sensor lifetime. The cost of producing LIG is low, due to the low cost of the chemicals used in the production process, the low entry cost of lasers typically used for LIG, and the scalability of the entire process. After work on device encapsulation and developing low-cost portable electronics, the commercialization process of such sensors could be relatively short, which makes their commercial use a viable prospect, after careful consideration of competing technologies.

In our previous work [14], we demonstrated wearable heartbeat sensors based on LIG sensing elements integrated with various flexible substrates. These sensors were analyzed using the open-source HeartPy toolkit for Python, a powerful tool primarily designed for processing photoplethysmography (PPG) signals. However, we have shown that HeartPy can also be effectively applied to LIG signals, particularly for extracting heart rate parameters [14]. By utilizing the HeartPy toolkit, we can derive several essential parameters, including heart rate, heart rate variability measures, as well as non-linear measurements, including Poincaré plot analysis. These parameters are highly valuable for medical analysis, offering useful insights into a patient's health condition. With further optimization, LIG/PU sensors could be utilized for respiratory rate tracking, tactile parameters, and oxygen saturation, demonstrating their potential for multi-functional medical wearables.

4. Conclusions

In summary, this study introduces a novel, flexible, biocompatible LIG/PU sensor with strong adhesion, mechanical stability, and electrical conductivity. Unlike conventional LIG devices fabricated on Kapton and transferred to PDMS with potential network damage [57], our approach yields devices with superior performance with simple fabrication, improved adhesion between LIG and PU and excellent signal-to-noise ratio.

The results demonstrate that the structural and mechanical properties of the PU substrates, governed by the SSC, significantly influence the quality of LIG transfer and the overall performance of the resulting composite materials.

The successful transfer of LIG onto PU substrates was achieved using spin coating and stamping, with spin coating yielding the best results for PUs with higher SSC. Specifically, PU substrates with 50 wt.% SSC (PU-50) showed superior compatibility with LIG, exhibiting higher transfer efficiency, reduced defect density, and improved structural integrity. In contrast, on PUs with lower SSC (PU-30 and PU-40) LIG transfer was partial or incomplete, particularly with the spin coating method, due to weaker adhesion and lower mechanical stability.

With FTIR spectroscopy we validated the chemical structures of PUs and confirmed the successful incorporation of LIG, while Raman spectroscopy revealed lower defect densities and enhanced crystallinity in LIG transferred onto PU-50 substrates. XRD analysis further supported these findings, showing a highly crystalline structure in the LIG/PU-50 samples, with interplanar distances consistent with literature values [8]. SEM and TEM confirmed the hierarchical porous morphology of LIG and highlighted its uniform distribution on PU-50 substrates.

Mechanical testing revealed that PU substrates with higher SSC provided an optimal balance of stiffness, hardness, and stretchability, with PU-50_{lo} demonstrating the best mechanical performance. The results underscore the critical role of substrate thickness and composition in determining the mechanical and functional properties of the LIG/PU

composites. The Scotch tape test results confirmed that PU-based substrates provide significantly stronger adhesion to LIG compared to commercial PI film, with PU-50 exhibiting the best performance due to its optimized balance of flexibility, mechanical stability, and chemical compatibility. The findings underscore the importance of selecting appropriate polymeric substrates for LIG-based flexible electronics and highlight PU-50 as a promising material for the development of durable and high-performance wearable sensors.

Pulse sensing tests showed that LIG/PU-50_{lo} achieved the highest signal-to-noise ratio (SNR = 270), significantly outperforming other fabricated LIG/PU, including LIG on PI. This superior performance can be attributed to optimized mechanical properties and small film thickness.

This study highlights the potential of LIG transferred onto biocompatible PU substrates as a promising material for wearable sensor applications, comparable to similar state-of-the-art devices [12–14]. The developed LIG/PU composites combine excellent flexibility, biocompatibility, strong adhesion, and mechanical stability, making them ideal for real-time health monitoring in medical and sports applications. Future work will explore the long-term durability and performance of these sensors under dynamic conditions to further expand their applicability in real-world scenarios.

Supplementary Materials: The following supporting information can be downloaded at: https://www.mdpi.com/article/10.3390/chemosensors13040122/s1, Figure S1: (a) Photographs of pure PU films; (b) UV-VIS spectra of thin pure PU films with different SSC. Figure S2: Cross-section micrograph of select LIG/PU-50 material. Table S1: EDX analysis data for atomic concentrations for LIG on different substrates. Table S2: Data obtained from Raman analysis: intensity ratio, LIG crystallite dimensions and FWHM for D, G and 2D peaks. Figure S3: Deconvolution of D and G region in Raman spectra. (a) LIG/PI, (b) LIG/PU-50_{lo}, (c) LIG/PU-50_{hi}, (d) LIG/PU-40, (e) LIG/PU-30_{sc} and (f) LIG/PU-30st. Table S3: Data obtained after the deconvolution of Raman D and G region (Figure S3). Figure S4: Deconvolution of 2D region in Raman spectra. (a) LIG/PI, (b) LIG/PU-50_{lo}, (c) LIG/PU-50_{hi}, (d) LIG/PU-40 and (e) LIG/PU-30_{sc}. Table S4: Data obtained from the deconvolution of 2D region in Raman spectra (Figure S4). Figure S5: Relationship between I_D/I_G ratio and crystallite dimensions in LIG transferred to different substrates. Figure S6: Original HRTEM images of LIG: (a) domain with parallel lines that correspond to d ~0.34 nm and (b) domain with parallel lines with d > 0.34 nm. Figure S7: XRD patterns of selected LIG/PU materials. Figure S8: Average load–displacement curves for all investigated materials. Figure S9: Photographs of the procedure for Scotch-tape test: (a) LIG/PI, (b) LIG/PU-30st, (c) LIG/PU-40 and (d) LIG/PU-50. Figure S10: Pulse sensing application of LIG/PU-50_{lo} sensor: repeated measurements of voltage variation in real time. Figure S11: Pulse sensing application of LIG/PU-50_{hi} sensor: repeated measurements of voltage variation in real time. Figure S12: Pulse sensing application of LIG/PU-40 sensor: repeated measurements of voltage variation in real time. Figure S13: Pulse sensing application of LIG/PI sensor: repeated measurements of voltage variation in real time.

Author Contributions: Conceptualization, M.V.P. and M.S.; methodology, M.V.P. and M.S.; validation, V.V., M.V.P., M.S., I.P., T.V., M.R.R. and S.D.I.; formal Analysis, V.V., M.V.P., M.S., I.P., T.V., M.R.R. and S.D.I.; investigation, V.V., M.V.P., M.S., I.P., T.V., M.R.R. and S.D.I.; resources, M.V.P. and M.S.; data curation, V.V., M.V.P., M.S., I.P., T.V., M.R.R. and S.D.I.; writing—original draft preparation, V.V. and M.V.P.; writing—review and editing, M.V.P. and M.S.; visualization, V.V. and M.V.P.; supervision, M.V.P. and M.S.; project administration, M.V.P. and M.S.; funding acquisition, M.S. All authors have read and agreed to the published version of the manuscript.

Funding: This research was supported by the Science Fund of the Republic of Serbia, #4950, Polymer/graphene heterostructures for physiological sensors—Polygraph and by the Ministry of Science, Technological Development, and Innovation of the Republic of Serbia (Contract No: 451-03-136/2025-03/200026).

Institutional Review Board Statement: Not applicable.

Informed Consent Statement: Not applicable.

Data Availability Statement: Data are contained within the article or Supplementary Materials.

Acknowledgments: The authors are grateful to: Olivera Živković (ICTM, University of Belgrade) for UV-VIS measurements; Marko V. Bošković (ICTM, University of Belgrade) for thickness measurements; Ivana Mladenović (ICTM, University of Belgrade) for adhesion test; Igor A. Pašti (Faculty of Physical Chemistry, University of Belgrade) for SEM/EDX analysis; Danica Bajuk-Bogdanović (Faculty of Physical Chemistry, University of Belgrade) for Raman spectroscopy and Gordana Tovilović-Kovačević (Institute for Biological Research "Siniša Stanković", University of Belgrade) for cytotoxicity test. Graphical abstract was created in BioRender: Vojnović, V. (2025) https://BioRender.com/v47q248 (accessed on 17 December 2024).

Conflicts of Interest: The authors declare no conflicts of interest.

References

1. Heikenfeld, J.; Jajack, A.; Rogers, J.; Gutruf, P.; Tian, L.; Pan, T.; Li, R.; Khine, M.; Kim, J.; Wang, J.; et al. Wearable Sensors: Modalities, Challenges, and Prospects. *Lab Chip* **2018**, *18*, 217–248. [CrossRef] [PubMed]
2. Lee, S.; Gandla, S.; Naqi, M.; Jung, U.; Youn, H.; Pyun, D.; Rhee, Y.; Kang, S.; Kwon, H.-J.; Kim, H.; et al. All-Day Mobile Healthcare Monitoring System Based on Heterogeneous Stretchable Sensors for Medical Emergency. *IEEE Trans. Ind. Electron.* **2020**, *67*, 8808–8816. [CrossRef]
3. Xue, Z.; Gai, Y.; Wu, Y.; Liu, Z.; Li, Z. Wearable Mechanical and Electrochemical Sensors for Real-Time Health Monitoring. *Commun. Mater.* **2024**, *5*, 211. [CrossRef]
4. Madevska Bogdanova, A.; Koteska, B.; Vićentić, T.; DIlić, S.; Tomić, M.; Spasenović, M. Blood Oxygen Saturation Estimation with Laser-Induced Graphene Respiration Sensor. *J. Sens.* **2024**, *2024*, 4696031. [CrossRef]
5. Luo, S.; Hoang, P.T.; Liu, T. Direct Laser Writing for Creating Porous Graphitic Structures and Their Use for Flexible and Highly Sensitive Sensor and Sensor Arrays. *Carbon* **2016**, *96*, 522–531. [CrossRef]
6. Luong, D.X.; Subramanian, A.K.; Silva, G.A.L.; Yoon, J.; Cofer, S.; Yang, K.; Owuor, P.S.; Wang, T.; Wang, Z.; Lou, J.; et al. Laminated Object Manufacturing of 3D-Printed Laser-Induced Graphene Foams. *Adv. Mater.* **2018**, *30*, 1707416. [CrossRef]
7. Chen, X.; Luo, F.; Yuan, M.; Xie, D.; Shen, L.; Zheng, K.; Wang, Z.; Li, X.; Tao, L. A Dual-Functional Graphene-Based Self-Alarm Health-Monitoring E-Skin. *Adv. Funct. Mater.* **2019**, *29*, 1904706. [CrossRef]
8. Lin, J.; Peng, Z.; Liu, Y.; Ruiz-Zepeda, F.; Ye, R.; Samuel, E.L.G.; Yacaman, M.J.; Yakobson, B.I.; Tour, J.M. Laser-Induced Porous Graphene Films from Commercial Polymers. *Nat. Commun.* **2014**, *5*, 5714. [CrossRef]
9. Chyan, Y.; Ye, R.; Li, Y.; Singh, S.P.; Arnusch, C.J.; Tour, J.M. Laser-Induced Graphene by Multiple Lasing: Toward Electronics on Cloth, Paper, and Food. *ACS Nano* **2018**, *12*, 2176–2183. [CrossRef]
10. Houeix, Y.; Romero, F.J.; Moraila, C.L.; Rivadeneyra, A.; Rodriguez, N.; Morales, D.P.; Salinas-Castillo, A. Laser-Synthesis of Conductive Carbon-Based Materials from Two Flexible Commercial Substrates: A Comparison. *Appl. Surf. Sci.* **2023**, *634*, 157629. [CrossRef]
11. Vićentić, T.; Greco, I.; Iorio, C.S.; Mišković, V.; Bajuk-Bogdanović, D.; Pašti, I.A.; Radulović, K.; Klenk, S.; Stimpel-Lindner, T.; Duesberg, G.S.; et al. Laser-Induced Graphene on Cross-Linked Sodium Alginate. *Nanotechnology* **2024**, *35*, 115103. [CrossRef] [PubMed]
12. Carvalho, A.F.; Fernandes, A.J.S.; Leitão, C.; Deuermeier, J.; Marques, A.C.; Martins, R.; Fortunato, E.; Costa, F.M. Laser-Induced Graphene Strain Sensors Produced by Ultraviolet Irradiation of Polyimide. *Adv. Funct. Mater.* **2018**, *28*, 1805271. [CrossRef]
13. Kaidarova, A.; Alsharif, N.; Oliveira, B.N.M.; Marengo, M.; Geraldi, N.R.; Duarte, C.M.; Kosel, J. Laser-Printed, Flexible Graphene Pressure Sensors. *Global Chall.* **2020**, *4*, 2000001. [CrossRef]
14. Vićentić, T.; Rašljić Rafajilović, M.; Ilić, S.D.; Koteska, B.; Madevska Bogdanova, A.; Pašti, I.A.; Lehocki, F.; Spasenović, M. Laser-Induced Graphene for Heartbeat Monitoring with HeartPy Analysis. *Sensors* **2022**, *22*, 6326. [CrossRef] [PubMed]
15. Zou, Y.; Zhong, M.; Li, S.; Qing, Z.; Xing, X.; Gong, G.; Yan, R.; Qin, W.; Shen, J.; Zhang, H.; et al. Flexible Wearable Strain Sensors Based on Laser-Induced Graphene for Monitoring Human Physiological Signals. *Polymers* **2023**, *15*, 3553. [CrossRef] [PubMed]
16. Liu, J.; Wu, D.; Liu, C.; Wang, Q.; Wang, H. Full-Range On-Body Strain Sensor of Laser-Induced Graphene Embedded in Thermoplastic Elastomer via Hot Pressing Transfer for Monitoring of the Physiological Signals. *Adv. Mater. Technol.* **2024**, *9*, 2301658. [CrossRef]
17. Abedheydari, F.; Sadeghzadeh, S.; Saadatbakhsh, M.; Heydariyan, A.; Khakpour, E. Silver-Decorated Laser-Induced Graphene for a Linear, Sensitive, and Almost Hysteresis-Free Piezoresistive Strain Sensor. *Sci. Rep.* **2024**, *14*, 28715. [CrossRef]
18. Zanoni, J.; Moura, J.P.; Santos, N.F.; Carvalho, A.F.; Fernandes, A.J.S.; Monteiro, T.; Costa, F.M.; Pereira, S.O.; Rodrigues, J. Dual Transduction of H_2O_2 Detection Using ZnO/Laser-Induced Graphene Composites. *Chemosensors* **2021**, *9*, 102. [CrossRef]

19. Zhang, S.; Liu, Y.; Wang, J.; Liu, Z. A Laser-Induced Photoelectrochemical Sensor for Natural Sweat Cu^{2+} Detection. *Chemosensors* **2022**, *10*, 169. [CrossRef]
20. Žutautas, V.; Trusovas, R.; Sartanavičius, A.; Ratautas, K.; Selskis, A.; Pauliukaite, R. A Sensor for Electrochemical pH Monitoring Based on Laser-Induced Graphene Modified with Polyfolate. *Chemosensors* **2023**, *11*, 329. [CrossRef]
21. Kulyk, B.; Silva, B.F.R.; Carvalho, A.F.; Silvestre, S.; Fernandes, A.J.S.; Martins, R.; Fortunato, E.; Costa, F.M. Laser-Induced Graphene from Paper for Mechanical Sensing. *ACS Appl. Mater. Interfaces* **2021**, *13*, 10210–10221. [CrossRef] [PubMed]
22. Bressi, A.C.; Dallinger, A.; Steksova, Y.; Greco, F. Bioderived Laser-Induced Graphene for Sensors and Supercapacitors. *ACS Appl. Mater. Interfaces* **2023**, *15*, 35788–35814. [CrossRef]
23. Getachew, B.A.; Bergsman, D.S.; Grossman, J.C. Laser-Induced Graphene from Polyimide and Polyethersulfone Precursors as a Sensing Electrode in Anodic Stripping Voltammetry. *ACS Appl. Mater. Interfaces* **2020**, *12*, 48511–48517. [CrossRef]
24. Mishra, N.K.; Patil, N.; Anas, M.; Zhao, X.; Wilhite, B.A.; Green, M.J. Highly Selective Laser-Induced Graphene (LIG)/Polysulfone Composite Membrane for Hydrogen Purification. *Appl. Mater. Today* **2021**, *22*, 100971. [CrossRef]
25. Vashisth, A.; Kowalik, M.; Gerringer, J.C.; Ashraf, C.; Van Duin, A.C.T.; Green, M.J. ReaxFF Simulations of Laser-Induced Graphene (LIG) Formation for Multifunctional Polymer Nanocomposites. *ACS Appl. Nano Mater.* **2020**, *3*, 1881–1890. [CrossRef]
26. Ghavipanjeh, A.; Sadeghzadeh, S. Simulation and Experimental Evaluation of Laser-Induced Graphene on the Cellulose and Lignin Substrates. *Sci. Rep.* **2024**, *14*, 4475. [CrossRef]
27. Parmeggiani, M.; Zaccagnini, P.; Stassi, S.; Fontana, M.; Bianco, S.; Nicosia, C.; Pirri, C.F.; Lamberti, A. PDMS/Polyimide Composite as an Elastomeric Substrate for Multifunctional Laser-Induced Graphene Electrodes. *ACS Appl. Mater. Interfaces* **2019**, *11*, 33221–33230. [CrossRef] [PubMed]
28. Wang, H.; Zhao, Z.; Liu, P.; Guo, X. A Soft and Stretchable Electronics Using Laser-Induced Graphene on Polyimide/PDMS Composite Substrate. *npj Flex. Electron.* **2022**, *6*, 26. [CrossRef]
29. Zaccagnini, P.; Ballin, C.; Fontana, M.; Parmeggiani, M.; Bianco, S.; Stassi, S.; Pedico, A.; Ferrero, S.; Lamberti, A. Laser-Induced Graphenization of PDMS as Flexible Electrode for Microsupercapacitors. *Adv. Mater. Interfaces* **2021**, *8*, 2101046. [CrossRef]
30. Lei Tang, J.Z.; Dawei Zhang, B.S. Laser-Induced Graphene Electrodes on Poly(Ether–Ether–Ketone)/PDMS Composite Films for Flexible Strain and Humidity Sensors. *ACS Appl. Nano Mater.* **2023**, *6*, 17802–17813. [CrossRef]
31. Pergal, M.V.; Rašljić Rafajilović, M.; Vićentić, T.; Pašti, I.A.; Ostojić, S.; Bajuk-Bogdanović, D.; Spasenović, M. Laser-Induced Graphene on Novel Crosslinked Poly(Dimethylsiloxane)/Triton X-100 Composites for Improving Mechanical, Electrical and Hydrophobic Properties. *Polymers* **2024**, *16*, 3157. [CrossRef] [PubMed]
32. Peng, Z.; Ye, R.; Mann, J.A.; Zakhidov, D.; Li, Y.; Smalley, P.R.; Lin, J.; Tour, J.M. Flexible Boron-Doped Laser-Induced Graphene Microsupercapacitors. *ACS Nano* **2015**, *9*, 5868–5875. [CrossRef] [PubMed]
33. Qiwen Zhang, F.Z.; Xing Liu, Z.Y.; Xi Chen, Z.W. Doping of Laser-Induced Graphene and Its Applications. *Adv. Mater. Technol.* **2023**, *8*, 2300244. [CrossRef]
34. Shin, B.S.; Oh, J.Y.; Sohn, H. Theoretical and Experimental Investigations into Laser Ablation of Polyimide and Copper Films with 355-Nm Nd:YVO4 Laser. *J. Mater. Process. Technol.* **2007**, *187–188*, 260–263. [CrossRef]
35. Wang, L.; Wang, Z.; Bakhtiyari, A.N.; Zheng, H. A Comparative Study of Laser-Induced Graphene by CO_2 Infrared Laser and 355 Nm Ultraviolet (UV) Laser. *Micromachines* **2020**, *11*, 1094. [CrossRef]
36. Dong, Y.; Rismiller, S.C.; Lin, J. Molecular Dynamic Simulation of Layered Graphene Clusters Formation from Polyimides under Extreme Conditions. *Carbon* **2016**, *104*, 47–55. [CrossRef]
37. Chen, Y.; Long, J.; Zhou, S.; Shi, D.; Huang, Y.; Chen, X.; Gao, J.; Zhao, N.; Wong, C. UV Laser-Induced Polyimide-to-Graphene Conversion: Modeling, Fabrication, and Application. *Small Methods* **2019**, *3*, 1900208. [CrossRef]
38. Duy, L.X.; Peng, Z.; Li, Y.; Zhang, J.; Ji, Y.; Tour, J.M. Laser-Induced Graphene Fibers. *Carbon* **2018**, *126*, 472–479. [CrossRef]
39. Hong, S.; Kim, J.; Jung, S.; Lee, J.; Shin, B.S. Surface Morphological Growth Characteristics of Laser-Induced Graphene with UV Pulsed Laser and Sensor Applications. *ACS Mater. Lett.* **2023**, *5*, 1261–1270. [CrossRef]
40. Li, Y.; Luong, D.X.; Zhang, J.; Tarkunde, Y.R.; Kittrell, C.; Sargunaraj, F.; Ji, Y.; Arnusch, C.J.; Tour, J.M. Laser-Induced Graphene in Controlled Atmospheres: From Superhydrophilic to Superhydrophobic Surfaces. *Adv. Mater.* **2017**, *29*, 1700496. [CrossRef]
41. Taşdemir, M.; Şenaslan, F.; Çelik, A. Investigation of Corrosion and Thermal Behavior of PU–PDMS-Coated AISI 316L. *e-Polymers* **2021**, *21*, 355–365. [CrossRef]
42. Chattopadhyay, D.K.; Webster, D.C. Thermal Stability and Flame Retardancy of Polyurethanes. *Prog. Polym. Sci.* **2009**, *34*, 1068–1133. [CrossRef]
43. Pergal, M.V.; Nestorov, J.; Tovilović, G.; Ostojić, S.; Gođevac, D.; Vasiljević-Radović, D.; Djonlagić, J. Structure and Properties of Thermoplastic Polyurethanes Based on Poly(Dimethylsiloxane): Assessment of Biocompatibility: Structure, Properties and Biocompatibility of TPUs. *J. Biomed. Mater. Res.* **2014**, *102*, 3951–3964. [CrossRef]
44. Ma, Z.; Khoo, B.L. Recent Advances in Laser-Induced-Graphene-Based Soft Skin Electronics for Intelligent Healthcare. *Soft Sci.* **2024**, *4*, 26. [CrossRef]

45. Pergal, M.V.; Antic, V.V.; Tovilovic, G.; Nestorov, J.; Vasiljevic-Radovic, D.; Djonlagic, J. In Vitro Biocompatibility Evaluation of Novel Urethane–Siloxane Co-Polymers Based on Poly(ϵ-Caprolactone)-*Block*-Poly(Dimethylsiloxane)-*Block*-Poly(ϵ-Caprolactone). *J. Biomater. Sci. Polym. Ed.* **2012**, *23*, 1629–1657. [CrossRef]
46. Pergal, M.V.; Brkljačić, J.; Tovilović-Kovačević, G.; Špírková, M.; Kodranov, I.D.; Manojlović, D.D.; Ostojić, S.; Knežević, N.Ž. Effect of Mesoporous Silica Nanoparticles on the Properties of Polyurethane Network Composites. *Prog. Org. Coat.* **2021**, *151*, 106049. [CrossRef]
47. Yilgör, I.; Yilgör, E.; Wilkes, G.L. Critical Parameters in Designing Segmented Polyurethanes and Their Effect on Morphology and Properties: A Comprehensive Review. *Polymer* **2015**, *58*, A1–A36. [CrossRef]
48. Velasco, A.; Ryu, Y.K.; Hamada, A.; De Andrés, A.; Calle, F.; Martinez, J. Laser-Induced Graphene Microsupercapacitors: Structure, Quality, and Performance. *Nanomaterials* **2023**, *13*, 788. [CrossRef]
49. Luong, D.X.; Yang, K.; Yoon, J.; Singh, S.P.; Wang, T.; Arnusch, C.J.; Tour, J.M. Laser-Induced Graphene Composites as Multifunctional Surfaces. *ACS Nano* **2019**, *13*, 2579–2586. [CrossRef]
50. Lamberti, A.; Clerici, F.; Fontana, M.; Scaltrito, L. A Highly Stretchable Supercapacitor Using Laser-Induced Graphene Electrodes onto Elastomeric Substrate. *Adv. Energy Mater.* **2016**, *6*, 1600050. [CrossRef]
51. Han, T.; Nag, A.; Simorangkir, R.B.V.B.; Afsarimanesh, N.; Liu, H.; Mukhopadhyay, S.C.; Xu, Y.; Zhadobov, M.; Sauleau, R. Multifunctional Flexible Sensor Based on Laser-Induced Graphene. *Sensors* **2019**, *19*, 3477. [CrossRef] [PubMed]
52. Zhu, J.; Cho, M.; Li, Y.; Cho, I.; Suh, J.-H.; Orbe, D.D.; Jeong, Y.; Ren, T.-L.; Park, I. Biomimetic Turbinate-like Artificial Nose for Hydrogen Detection Based on 3D Porous Laser-Induced Graphene. *ACS Appl. Mater. Interfaces* **2019**, *11*, 24386–24394. [CrossRef]
53. Dallinger, A.; Keller, K.; Fitzek, H.; Greco, F. Stretchable and Skin-Conformable Conductors Based on Polyurethane/Laser-Induced Graphene. *ACS Appl. Mater. Interfaces* **2020**, *12*, 19855–19865. [CrossRef] [PubMed]
54. Griesche, C.; Hoecherl, K.; Baeumner, A.J. Substrate-Independent Laser-Induced Graphene Electrodes for Microfluidic Electroanalytical Systems. *ACS Appl. Nano Mater.* **2021**, *4*, 3114–3121. [CrossRef]
55. Li, J.T.; Stanford, M.G.; Chen, W.; Presutti, S.E.; Tour, J.M. Laminated Laser-Induced Graphene Composites. *ACS Nano* **2020**, *14*, 7911–7919. [CrossRef] [PubMed]
56. Gholami, R.; Lawan, I.; Luengrojanakul, P.; Ebrahimi, S.; Ahn, C.-H.; Rimdusit, S. Development of a Laser Induced Graphene (LIG) and Polylactic Acid (PLA) Shape Memory Polymer Composite with Simultaneous Multi-Stimuli Response and Deformation Self-Sensing Characteristics. *Nanoscale Adv.* **2024**, *6*, 4865–4876. [CrossRef] [PubMed]
57. Rahimi, R.; Ochoa, M.; Yu, W.; Ziaie, B. Highly Stretchable and Sensitive Unidirectional Strain Sensor via Laser Carbonization. *ACS Appl. Mater. Interfaces* **2015**, *7*, 4463–4470. [CrossRef]
58. Raza, T.; Tufail, M.K.; Ali, A.; Boakye, A.; Qi, X.; Ma, Y.; Ali, A.; Qu, L.; Tian, M. Wearable and Flexible Multifunctional Sensor Based on Laser-Induced Graphene for the Sports Monitoring System. *ACS Appl. Mater. Interfaces* **2022**, *48*, 54170–54181. [CrossRef]
59. Huang, L.; Wang, H.; Wu, P.; Huang, W.; Gao, W.; Fang, F.; Cai, N.; Chen, R.; Zhu, Z. Wearable Flexible Strain Sensor Based on Three-Dimensional Wavy Laser-Induced Graphene and Silicone Rubber. *Sensors* **2020**, *20*, 4266. [CrossRef]
60. Wang, W.; Lu, L.; Xie, Y.; Yuan, W.; Wan, Z.; Tang, Y.; Teh, K.S. A Highly Stretchable Microsupercapacitor Using Laser-Induced Graphene/NiO/Co_3O_4 Electrodes on a Biodegradable Waterborne Polyurethane Substrate. *Adv. Mater. Technol.* **2020**, *5*, 1900903. [CrossRef]
61. Lu, Y.; Yang, G.; Wang, S.; Zhang, Y.; Jian, Y.; He, L.; Yu, T.; Luo, H.; Kong, D.; Xianyu, Y.; et al. Stretchable Graphene–Hydrogel Interfaces for Wearable and Implantable Bioelectronics. *Nat. Electron.* **2023**, *7*, 51–65. [CrossRef]
62. Marand, Å.; Dahlin, J.; Karlsson, D.; Skarping, G.; Dalene, M. Determination of Technical Grade Isocyanates Used in the Production of Polyurethane Plastics. *J. Environ. Monitor* **2004**, *6*, 606. [CrossRef]
63. Petrović, Z.; Ferguson, J. Polyurethane Elastomers. *Prog. Polym. Sci.* **1991**, *16*, 695–836. [CrossRef]
64. Tuinstra, F.; Koenig, J.L. Raman Spectrum of Graphite. *J. Chem. Phys.* **1970**, *53*, 1126–1130. [CrossRef]
65. Pergal, M.V.; Antić, V.; Ostojić, S.; Marinović-Cincović, M.; Djonlagić, J. Influence of the Content of Hard Segments on the Properties of Novel Urethane-Siloxane Copolymers Based on a Poly(ε-Caprolactone)-b-Poly(Dimethylsiloxane)-b-Poly(ε- Caprolactone) Triblock Copolymer. *J. Serb. Chem. Soc.* **2011**, *76*, 1703–1723. [CrossRef]
66. Van Gent, P.; Farah, H.; Van Nes, N.; Van Arem, B. HeartPy: A Novel Heart Rate Algorithm for the Analysis of Noisy Signals. *Transp. Res. F Traffic Psychol. Behav.* **2019**, *66*, 368–378. [CrossRef]
67. Gordon, S.H.; Mohamed, A.; Harry-O'kuru, R.E.; Imam, S.H. A Chemometric Method for Correcting Fourier Transform Infrared Spectra of Biomaterials for Interference from Water in KBr Discs. *Appl. Spectrosc.* **2010**, *64*, 448–457. [CrossRef]
68. Yogesh, G.K.; Gumpu, M.B.; Shuaib, E.P.; Sastikumar, D. Laser-Induced Transformation of Graphene into Graphene Oxide Nanospheres (GONs). *Mater. Res. Bull.* **2019**, *115*, 227–234. [CrossRef]
69. Khalili, D. Graphene Oxide: A Promising Carbocatalyst for the Regioselective Thiocyanation of Aromatic Amines, Phenols, Anisols and Enolizable Ketones by Hydrogen Peroxide/KSCN in Water. *New J. Chem.* **2016**, *40*, 2547–2553. [CrossRef]
70. Sindhu, B.; Kothuru, A.; Sahatiya, P.; Goel, S.; Nandi, S. Laser-Induced Graphene Printed Wearable Flexible Antenna-Based Strain Sensor for Wireless Human Motion Monitoring. *IEEE Trans. Electron. Devices* **2021**, *68*, 3189–3194. [CrossRef]

71. Pergal, M.; Dzunuzovic, J.; Spírková, M.; Poręba, R.; Steinhart, M.; Pergal, M.; Ostojic, S. Study on the Morphology and Thermomechanical Properties of Poly(Urethane-Siloxane) Networks Based on Hyperbranched Polyester. *Hem. Ind.* **2013**, *67*, 871–879. [CrossRef]
72. Peña-Álvarez, M.; Corro, E.D.; Langa, F.; Baonza, V.G.; Taravillo, M. Morphological Changes in Carbon Nanohorns under Stress: A Combined Raman Spectroscopy and TEM Study. *RSC Adv.* **2016**, *6*, 49543–49550. [CrossRef]
73. Claramunt, S.; Varea, A.; López-Díaz, D.; Velázquez, M.M.; Cornet, A.; Cirera, A. The Importance of Interbands on the Interpretation of the Raman Spectrum of Graphene Oxide. *J. Phys. Chem. C* **2015**, *119*, 10123–10129. [CrossRef]
74. Ferrari, A.C.; Robertson, J. Interpretation of Raman Spectra of Disordered and Amorphous Carbon. *Phys. Rev. B* **2000**, *61*, 14095–14107. [CrossRef]
75. Pergal, M.; Dzunuzovic, J.; Ostojic, S.; Pergal, M.; Radulovic, A.; Jovanovic, S. Poly(Urethane-Siloxane)s Based on Hyperbranched Polyester as Crosslinking Agent: Synthesis and Characterization. *J. Serb. Chem. Soc.* **2012**, *77*, 919–935. [CrossRef]
76. Hwangbo, Y.; Lee, C.-K.; Mag-Isa, A.E.; Jang, J.-W.; Lee, H.-J.; Lee, S.-B.; Kim, S.-S.; Kim, J.-H. Interlayer Non-Coupled Optical Properties for Determining the Number of Layers in Arbitrarily Stacked Multilayer Graphenes. *Carbon* **2014**, *77*, 454–461. [CrossRef]
77. Ferrari, A.C.; Meyer, J.C.; Scardaci, V.; Casiraghi, C.; Lazzeri, M.; Mauri, F.; Piscanec, S.; Jiang, D.; Novoselov, K.S.; Roth, S.; et al. Raman Spectrum of Graphene and Graphene Layers. *Phys. Rev. Lett.* **2006**, *97*, 187401. [CrossRef]
78. Bleu, Y.; Bourquard, F.; Loir, A.; Barnier, V.; Garrelie, F.; Donnet, C. Raman Study of the Substrate Influence on Graphene Synthesis Using a Solid Carbon Source via Rapid Thermal Annealing. *J. Raman Spectrosc.* **2019**, *50*, 1630–1641. [CrossRef]
79. Cheng, L.; Yeung, C.S.; Huang, L.; Ye, G.; Yan, J.; Li, W.; Yiu, C.; Chen, F.-R.; Shen, H.; Tang, B.Z.; et al. Flash Healing of Laser-Induced Graphene. *Nat. Commun.* **2024**, *15*, 2925. [CrossRef]
80. Cao, L.; Zhu, S.; Pan, B.; Dai, X.; Zhao, W.; Liu, Y.; Xie, W.; Kuang, Y.; Liu, X. Stable and Durable Laser-Induced Graphene Patterns Embedded in Polymer Substrates. *Carbon* **2020**, *163*, 85–94. [CrossRef]
81. Menon, D.M.N.; Giardino, M.; Janner, D. Direct Fabrication of Ultrahydrophobic Laser-Induced Graphene for Strain Sensors. *Appl. Sci.* **2023**, *13*, 4935. [CrossRef]
82. Zafar, M.A.; Liu, Y.; Jacob, M.V. Green Synthesis of Graphene for Targeted Recovery of Silver from Photovoltaic Waste. *Chemosphere* **2024**, *362*, 142512. [CrossRef]
83. Cheng, Y.; Zhou, S.; Hu, P.; Zhao, G.; Li, Y.; Zhang, X.; Han, W. Enhanced Mechanical, Thermal, and Electric Properties of Graphene Aerogels via Supercritical Ethanol Drying and High-Temperature Thermal Reduction. *Sci. Rep.* **2017**, *7*, 1439. [CrossRef]
84. Singh, S.P.; Li, Y.; Zhang, J.; Tour, J.M.; Arnusch, C.J. Sulfur-Doped Laser-Induced Porous Graphene Derived from Polysulfone-Class Polymers and Membranes. *ACS Nano* **2018**, *12*, 289–297. [CrossRef]
85. Xiaojuan, L.; Xiaorui, L.; Lei, W.; Yiding, S. Synthesis and Characterizations of Waterborne Polyurethane Modified with 3-Aminopropyltriethoxysilane. *Polym. Bull.* **2010**, *65*, 45–57. [CrossRef]
86. Yan, R.; Liu, Y.; Liu, B.; Zhang, Y.; Zhao, Q.; Sun, Z.; Hu, W.; Zhang, N. Improved Performance of Dual-Cured Organosolv Lignin-Based Epoxy Acrylate Coatings. *Compos. Commun.* **2018**, *10*, 52–56. [CrossRef]
87. Hormaiztegui, M.E.V.; Mucci, V.L.; Aranguren, M.I. Composite Films Obtained from a Waterborne Biopolyurethane. Incorporation of Tartaric Acid and Nanocellulose. *Ind. Crops Prod.* **2019**, *142*, 111879. [CrossRef]
88. Greenwood, J.A.; Williamson, J.B.P. Contact of Nominally Flat Surfaces. *Proc. R. Soc. A Math. Phys. Eng. Sci.* **1966**, *295*, 300–319. [CrossRef]
89. Tanaka, K. Elastic/Plastic Indentation Hardness and Indentation Fracture Toughness: The Inclusion Core Model. *J. Mater. Sci.* **1987**, *22*, 1501–1508. [CrossRef]
90. Kirkpatrick, C.J.; Otto, M.; Kooten, T.V.; Krump, V.; Kriegsmann, J.; Bittinger, F. Endothelial Cell Cultures as a Tool in Biomaterial Research. *J. Mater. Sci. Mater. Med.* **1999**, *10*, 589–594. [CrossRef]
91. Fei, X.; Huang, J.; Shi, W. Humidity Sensor Composed of Laser-Induced Graphene Electrode and Graphene Oxide for Monitoring Respiration and Skin Moisture. *Sensors* **2023**, *23*, 6784. [CrossRef] [PubMed]
92. Felineger, A. *Data Analysis and Signal Processing in Chromatography*; Elsevier: Amsterdam, The Netherlands, 1998; Chapter 6; pp. 125–141.

Disclaimer/Publisher's Note: The statements, opinions and data contained in all publications are solely those of the individual author(s) and contributor(s) and not of MDPI and/or the editor(s). MDPI and/or the editor(s) disclaim responsibility for any injury to people or property resulting from any ideas, methods, instructions or products referred to in the content.